Title
Feedback generates a second receptive field in neurons of the visual cortex

Journal
Nature, 582(7813)

ISSN
0028-0836

Authors
Keller, Andreas J
Roth, Morgane M
Scanziani, Massimo

Publication Date
2020-06-25

DOI
10.1038/s41586-020-2319-4

Peer reviewed

HHS Public Access

Author manuscript

Nature. Author manuscript; available in PMC 2021 January 07.

Published in final edited form as:

Nature. 2020 June ; 582(7813): 545–549. doi:10.1038/s41586-020-2319-4.

Feedback Generates a Second Receptive Field in Neurons of Visual Cortex

Andreas J Keller[1,2,*], **Morgane M Roth**[1,2], **Massimo Scanziani**[1,2,*]

[1]Department of Physiology, University of California San Francisco, San Francisco, California, USA.

[2]Howard Hughes Medical Institute, University of California San Francisco, San Francisco, California, USA.

Abstract

We sense our environment through pathways linking sensory organs to the brain. In the visual system, these feedforward pathways define the classical feedforward receptive field (ffRF), the area in space where visual stimuli excite a neuron[1]. The visual system also uses visual context, the visual scene surrounding a stimulus, to predict the content of the stimulus[2], and accordingly, neurons have been found that are excited by stimuli outside their ffRF[3–8]. The mechanisms generating excitation to stimuli outside the ffRF are, however, unclear. Here we show that feedback projections onto excitatory neurons in mouse primary visual cortex (V1) generate a second receptive field driven by stimuli outside the ffRF. Stimulating this feedback receptive field (fbRF) elicits slow and delayed responses compared to ffRF stimulation. These responses are preferentially reduced by anesthesia and, importantly, by silencing higher visual areas (HVAs). Feedback inputs from HVAs have scattered receptive fields relative to their putative V1 targets enabling the generation of the fbRF. Neurons with fbRFs are located in cortical layers receiving strong feedback projections and are absent in the main input layer, consistent with a laminar processing hierarchy. The fbRF and the ffRF are mutually antagonistic since large, uniform stimuli, covering both, suppress responses. While somatostatin-expressing (SOM) inhibitory neurons are driven by these large stimuli, parvalbumin (PV) and vasoactive-intestinal-peptide-expressing (VIP) inhibitory neurons have antagonistic fbRF and ffRF, similar to excitatory neurons. Therefore, feedback projections may enable neurons to use context to predict information missing from the ffRF and to report differences in stimulus features across visual space, regardless if excitation occurs inside or outside the ffRF. We have identified a fbRF which, by complementing the ffRF, may contribute to predictive processing.

[*]All requests for materials and correspondence should be addressed to M.S. or A.J.K., andreasjakob.keller@ucsf.edu; massimo@ucsf.edu.

Author contributions. A.J.K. and M.S. designed the study. A.J.K. and M.M.R. conducted all experiments and analysis. M.S., A.J.K. and M.M.R wrote the manuscript.

The authors declare no competing interests.

Data availability. Datasets supporting the findings of this paper are available on request from the corresponding authors.

Code availability. Custom code is available from the corresponding authors on request.

To characterize the ffRF, we mapped receptive field (RF) locations of layer 2/3 (L2/3) excitatory neurons in V1 of awake head-fixed mice with two-photon calcium imaging (Fig. 1a). We determined the center of a neuron's ffRF using circular patches of drifting gratings presented individually at different locations (Fig. 1b). To estimate the size of the neuron's ffRF, we obtained a size-tuning function by varying the diameter of the grating (Fig. 1c) centered on the neuron's ffRF and at the neuron's preferred orientation. The responses were maximal for gratings of 13.1 ± 0.4° in diameter and were suppressed with increasing grating size (Fig 1c), consistent with previous reports[9–12].

To determine the spatial extent of the suppressive regions, we presented a full-field grating in which a portion was masked by a gray circular patch (Fig. 1a, b). We reasoned that the neuron's response would partially recover by placing the gray patch on a suppressive region, i.e. when part of the suppressive region is not stimulated. We varied the gray patch location along the same grid used to determine the neuron's ffRF location. We obtained two separate population-averaged activity maps, the ffRF map and the suppressive regions' map. Unexpectedly, the peak of these two maps overlapped (Fig. 1b). Thus, the largest recovery from suppression occurred when the gray patch was located at the center of the ffRF.

To obtain a finer measure of a neuron's response to a gray patch, we placed the patch on the center of the neuron's ffRF and varied its diameter. Even the smallest tested size (5°) evoked a response that was larger than that to the full-field grating. Strikingly, neuronal responses first increased and then decreased with the size of the gray patch (Fig. 1c). These responses were not due to the sharp edges of the stimuli since we observed similar responses when blurring the edges (Extended Data Fig. 1). Thus, the size-tuning function of a gray patch on a full-field grating (inverse stimulus) was similar to that of a grating patch on a gray background (classical stimulus).

These results show that L2/3 excitatory neurons are excited by both classical and inverse stimuli centered on their ffRF. Classical and inverse stimuli were mutually antagonistic because the responses to both stimuli together (e.g. full-field gratings) were smaller than the responses to either of the stimuli alone (Fig. 1c). We defined a neuron as inverse tuned if its response to at least one inverse stimulus of any size centered on its ffRF was larger than that to a full-field stimulus (see Methods). Of the visually responsive excitatory neurons in L2/3, 79% were inverse tuned (943 of 1190 neurons in 9 mice; Fig. 1a–c and Extended Data Fig. 2, 3a). We computed the inverse tuning index (ITI; 0.5: equal responses to classical and inverse stimuli of preferred size; 0: classical only; 1: inverse only; see Methods). The ITI distribution of L2/3 excitatory neurons was unimodal peaking at 0.52 ± 0.01 (mean ± SEM; Fig 1c).

Inverse-tuned neurons have a region surrounding their ffRF that is either suppressive or excitatory depending on whether it is stimulated in the presence or absence of a stimulus in the ffRF, respectively. We used classical and inverse stimuli to compare the tuning properties of the surrounding excitatory region with those of the ffRF. On average, the orientation tuning to inverse stimuli was sharper than that to classical stimuli (Extended Data Fig. 3b–f). Moreover, individual neurons were not necessarily tuned to the same orientation when stimulated by classical or inverse stimuli (Extended Data Fig. 3g). We determined the

interaction between the surrounding region and the ffRF in neurons with similar orientation preference by varying the contrast of classical or inverse stimuli presented simultaneously. With matching contrasts above 13% the interaction between the surrounding region and the ffRF was antagonistic (Extended Data Fig. 3h).

Is inverse tuning in L2/3 inherited from earlier stages of cortical processing? We measured the responses of excitatory neurons in layer 4 (L4) to classical and inverse stimuli (Fig. 1d–f, Extended Data Fig. 3i). In contrast to L2/3 neurons, the suppressive regions of L4 neurons surrounded their ffRF, creating a ring around the center (Fig. 1e; the absence of a suppressive ring around the ffRF of L2/3 neurons was not due to insufficient spatial resolution of the mapping stimuli; Extended Data Fig. 4). Further, the responses of L4 neurons to inverse stimuli placed on the ffRF center decreased monotonically with stimulus size, consistent with the progressive reduction of feedforward drive (Extended Fig. 2) and, again, different from L2/3 neurons (Fig. 1c vs Fig. 1f). Overall, the spatial organization of suppressive regions of L4 neurons was consistent with previous models and observations[7,13] and distinct from L2/3 neurons. Thus, inverse tuning in L2/3 excitatory neurons is not inherited from L4 neurons.

Sources of input to L2/3 neurons are neuron-type specific[11,14]. Is inverse tuning also present in L2/3 inhibitory neurons? We characterized the responses of the three major classes of cortical inhibitory neurons, PV, VIP and SOM neurons to classical and inverse stimuli (Fig. 2, Extended Data Fig. 3j–l). Both PV and VIP neurons showed surround suppression to classical stimuli, consistent with previous reports[11,15]. Furthermore, both PV and VIP neurons responded to inverse stimuli centered on their ffRF (Fig. 2b, c) and showed size-tuning functions to inverse stimuli that peaked well above their response to the largest classical stimuli. In contrast, SOM neurons only showed little surround suppression to classical stimuli[11,15], poor and spatially diffuse responses to inverse stimuli (Fig. 2d), and no responses to inverse stimuli above the response to the largest classical stimuli. Thus, like L2/3 excitatory neurons, most PV and VIP neurons were inverse tuned, while SOM neurons were not (Fig. 2).

Although L2/3 neurons do not directly inherit inverse tuning from L4, the excitatory region surrounding their ffRF could still be generated via feedforward inputs from L4 neurons with spatially offset ffRFs (Fig. 3a). Alternatively, the excitatory region surrounding L2/3 neurons' ffRFs could be generated via feedback projections[16,17]. We thus compared the latency of the responses of inverse-tuned neurons to classical and inverse stimuli using extracellular electrophysiological recordings (Fig. 3a) and isolated single units throughout cortical layers, including infragranular layers (L5/6). A large fraction of infragranular units were also inverse tuned (Extended Data Fig. 5). In inverse-tuned units recorded in both supra- and infragranular layers the time course of the responses to classical and inverse stimuli were markedly different (Fig. 3b). While the response to classical stimuli showed a fast initial transient followed by a plateau, the response to inverse stimuli slowly progressed towards steady state (Fig. 3c–e) and was delayed relative to the classical response (50 ± 20 ms; mean ± SEM; 15 units; Fig. 3f). The same biases were observed when comparing the response dynamics to classical stimuli in all responsive neurons to those to inverse stimuli in inverse-tuned neurons (Fig. 3g). The difference in latencies and the slower dynamics of

responses to inverse stimuli suggest that the excitatory region surrounding L2/3 neurons' ffRF is unlikely to emerge from the feedforward pathway.

Could the responses to inverse stimuli depend on feedback projections from higher visual areas (HVAs)? The impact of anesthesia on sensory responses has been hypothesized to be stronger in HVAs than in V1[18]. We thus compared the impact of isoflurane on the responses to classical stimuli in V1 and HVAs identified beforehand using wide-field intrinsic imaging (Extended Data Fig. 6a–c). Indeed, anesthesia suppressed responses more in HVAs than in V1 (Extended Data Fig. 6d–f). If responses of L2/3 neurons to inverse stimuli rely on feedback projections, they should be more sensitive to anesthesia than responses to classical stimuli. Indeed, in inverse-tuned neurons, anesthesia preferentially suppressed responses to inverse stimuli (Fig. 4), suggesting that the response to inverse stimuli may be driven by feedback projections from HVAs.

To directly test the involvement of feedback projections on inverse tuning, we silenced HVAs by scanning them with a laser to optogenetically activate inhibitory neurons, while recording extracellular electrophysiological activity in V1 (Fig. 5a–e and Extended Data Fig. 7a–c). In inverse-tuned units, silencing HVAs reduced both spontaneous activity and responses to small diameter classical stimuli. In surround-suppressed units, silencing HVAs increased responses to large diameter classical stimuli (Fig. 5b–d; Extended Data Fig. 8), as previously shown[19–21]. The response to inverse stimuli, however, was strongly suppressed (Fig. 5b–e). Upon silencing HVAs, inverse stimuli evoked responses that decreased with increasing size of the gray patch, reminiscent of L4. These effects could not be explained by a direct impact of scattered laser light on V1 (Extended Data Fig. 7d–g), and neither by the activation of putative inhibitory neurons in HVA with long range axonal projections targeting V1 since these projections were rare (Extended Data Fig. 7h–l), consistent with a previous study[22].

To test whether distinct HVAs contribute equally to inverse responses in V1 we silenced individual HVAs while recording single unit responses in V1 to classical and inverse stimuli (Extended Data Fig. 9). While the silencing of several visual areas reduced the response to inverse stimuli, the strongest stimulus-specific effect on inverse responses occurred when silencing the lateromedial visual area (LM).

Is inverse tuning directly inherited from inverse-tuned neurons in LM? We determined the responses properties of LM axonal boutons in layer 1 of V1 while mapping the retinotopic coordinates of the V1 site (Fig. 5f–i; Extended Data Fig. 10a–h). LM boutons whose RFs were centered on the retinotopic coordinates of the imaged V1 site, showed surround suppression to classical stimuli and were not inverse tuned (Fig. 5g). When presenting inverse stimuli centered on the RF of the LM boutons, the response decreased with increasing diameter of the gray patch, as in L4 neurons (Fig. 1f). This was not a general property of LM neurons since directly imaging cell bodies in LM showed inverse tuning in some neurons, and in the population average (Extended Data Fig. 10i–k). Thus, V1 neurons do not directly inherit inverse tuning from LM.

Inverse tuning of L2/3 neurons could result from LM inputs which, while *per se* not inverse tuned, have spatially offset RFs relative to those of L2/3 neurons. These LM inputs would respond to an inverse stimulus centered on the V1 retinotopic coordinates because their RF, being offset relative to the gray patch, would be stimulated by the grating. We mapped the spatial offset of the RF of LM boutons relative to the retinotopic coordinates of the V1 sites. The RF centers of LM boutons showed a wide scatter relative to the retinotopic coordinates of the V1 site, larger than the scatter of ffRF centers of L2/3 neurons at the V1 site (Fig. 5h; Extended Data Fig. 10f, g), consistent with a previous study[23]. Thus, LM boutons with spatially offset RF centers converge on a given retinotopic site in V1. If these LM inputs contribute to the inverse response of L2/3 neurons, they should respond to inverse stimuli centered on the V1 site. This was indeed the case on average and a large fraction of these boutons significantly responded to inverse stimuli (Extended Data Fig. 10h) with a preference for small sizes (Fig. 5i), consistent with the inverse size-tuning function in L2/3 neurons (Fig. 1c). In addition, the response of these boutons to progressively larger classical stimuli centered on the V1 site increased gradually (Fig. 5i), consistent with their RFs being offset relative to the center of the stimulus. Thus, inverse tuning in L2/3 V1 neurons likely results from the feedback of non-inverse-tuned neurons in HVAs whose RFs are offset relative to the ffRF centers of the V1 neurons they converge on.

Our results demonstrate that feedback projections to V1 neurons generate a second, distinct excitatory RF that surrounds the ffRF. This feedback RF (fbRF) is absent in L4 and emerges along the laminar processing hierarchy in the supra- and infragranular layers of V1. The fbRF and the ffRF are mutually antagonistic such that neurons respond when a stimulus is presented in either the fbRF or ffRF but not in both together, effectively performing an exclusive-OR operation. Suppression of responses to stimuli in the ffRF by surrounding stimuli is a well-established phenomenon that enables neurons to report differences in stimulus features between the excited region inside the ffRF and its surround[7,8,11,12,24–27]. Neurons with an excitatory fbRF report differences in stimulus features regardless of whether the excited region is located inside or outside the ffRF. We hypothesize that SOM inhibitory neurons, which, in contrast to PV and VIP neurons, respond poorly to inverse stimuli while robustly responding to large stimuli covering both fbRFs and ffRFs, could mediate the mutual antagonism consistent with their role in surround suppression[11].

In addition to HVAs, local excitation within V1 may also contribute to the generation of the fbRF[28,29]. Regardless, the fbRF may underlie phenomena such as filling-in or illusory contours in which the stimulus in the ffRF is absent, weak or obstructed[3,5,30–32] and may account for contextual modulation[8,12,24,27,33], detection of borders[6,7] or pop-out effects[34].

The antagonism between ffRF and fbRF is reminiscent of models of predictive processing[35–37] in which bottom-up information about the stimulus is compared with top-down predictions, such that only differences between prediction and stimulus identity are represented. Surround suppression has been interpreted within this framework because if the visual stimulus surrounding the ffRF predicts the stimulus in the ffRF there is no difference between prediction and stimulus identity and, therefore, the response is suppressed[36]. With inverse tuning, the framework of predictive processing generalizes to stimuli within and outside of the ffRF due to the presence of a fbRF. Independent of any conceptual framework,

the presence of a fbRF generated by feedback projections likely accounts for several aspects of sensory processing along the cortical hierarchy.

Methods

Animals.

All experimental procedures were approved by the regulation of the Institutional Animal Care and Use Committee (IACUC #AN179056) of the University of California, San Francisco. Mice of either sex were kept on a C57BL/6 background (except VIP-IRES-cre) and were of the following genotype:

Gad2-IRES-cre (GAD2$^{tm2(cre)Zjh}$; JAX:010802) × Ai14 (Gt(ROSA)26Sor$^{tm14(CAG-tdTomato)Hze}$; JAX:007914) for imaging of layer 2/3 (L2/3) excitatory neurons (9 mice; Fig. 1a–c and 4, Extended Data Fig. 1, 3, and 4); Emx1-IRES-cre (Emx1$^{tm1(cre)Krj}$; JAX:005628) for imaging L2/3 excitatory neurons and axons from LM (5 mice; Fig. 5f–i, and Extended Data Fig. 10a–h); Gad2-IRES-cre (GAD2$^{tm2(cre)Zjh}$; JAX:010802) for imaging L2/3 neurons and labelling inhibitory projections (8 mice; Extended Data Fig. 6, 7h–k, and 10i–k); PV-cre (Pvalb$^{tm1(cre)Arbr}$; JAX:017320) × Ai14 (Gt(ROSA)26Sor$^{tm14(CAG-tdTomato)Hze}$; JAX:007914) for imaging of L2/3 parvalbumin-expressing inhibitory neurons (PV; 7 mice; Fig. 2b); VIP-IRES-cre (Vip$^{tm1(cre)Zjh}$; JAX: 010908) × Ai14 (Gt(ROSA)26Sor$^{tm14(CAG-tdTomato)Hze}$; JAX:007914) for imaging of L2/3 vasoactive-intestinal-peptide-expressing inhibitory neurons (VIP; 8 mice; Fig. 2c); Sst-IRES-cre (Sst$^{tm2.1(cre)Zjh}$; JAX:028864) × Ai14 (Gt(ROSA)26Sor$^{tm14(CAG-tdTomato)Hze}$; JAX:007914) for imaging of L2/3 somatostatin-expressing inhibitory neurons (SOM; 5 mice; Fig. 2d); Scnn1a-Tg3-cre (Tg(Scnn1a-cre)3Aibs/J; JAX:009613) and Scnn1a-Tg3-cre (Tg(Scnn1a-cre)3Aibs/J; JAX:009613) × Ai148 (Igs7$^{tm148.1(tetO-GCaMP6f,CAG-tTA2)Hze}$; JAX:030328) for imaging layer 4 (L4) excitatory neurons (5 mice and 1 mouse, respectively; Fig. 1d–f, and Extended Data Fig. 4d); and VGAT-ChR2-EYFP (Tg(Slc32a1-COP4*H134R/EYFP)8Gfng/J; JAX:014548) for electrophysiology and optogenetic inhibition experiments (20 mice; Fig. 3 and 5a–e, Extended Data Fig. 5, 7a–g, 8, and 9). The mice were housed on a reverse light cycle (light/dark cycle: 12/12 hrs). At the start of the experiments, all mice were between 2 and 9 months old.

Viruses.

We injected the following viruses: AAV2/1.ef1a.GCaMP6f.WPRE (FMI Vector Core Facility), AAV2/1.ef1a.DIO.GCaMP6f.WPRE (FMI Vector Core Facility), AAV2/1.CAG.CGaMP6f (Janelia Vector Core), AAV2/9.syn.GCaMP7f (Addgene), AAV1.Syn.Flex.NES-jRGECO1a.WPRE.SV40 (Addgene) and AAVretro.CAG.Flex.tdTomato (Addgene). Viruses were diluted to use titers of approximately 5×10^{12} genome copies/ml and 50nl were injected at each injection site (3 to 5 for two-photon and 1 for anatomy experiments) and each depth (2 from 350 to 200 μm below the pial surface for two-photon calcium imaging experiments; 4 from 650 to 200 μm below the pial surface for the anatomy experiments and two-photon recordings of LM boutons).

Surgery.

Mice were anesthetized with 2% isoflurane or with a mixture of Fentanyl (West-Ward Pharmaceuticals, 0.05 mg/kg), Midazolam (Akorn, 5.0 mg/kg) and Dexmedetomidine (Zoetis, 0.5 mg/kg), injected subcutaneously. Mice's body temperature was monitored and kept constant. To prevent the eyes from drying, a layer of lubricant ointment (Rugby) was applied. The skin above the skull was disinfected with povidone iodine. For mice prepared for intrinsic optical imaging (those needed for two-photon calcium imaging in higher visual areas (HVAs) or in LM boutons, and for all electrophysiology experiments), the bone over the right visual cortex was thinned, the exposed skull was covered with a thin layer of glue (krazy glue) and a headplate was attached using dental cement (Ortho-Jet Powder, Lang). The mice were then allowed to recover for several days before any other surgical or experimental procedures. For two-photon experiments, a craniotomy was made over the right visual cortex (3 to 4.5 mm in diameter) and viruses were injected with a micropump (UMP-3, World Precision Instruments) at a rate of 2 nl/s. The craniotomy was then sealed with a glass coverslip using cyanoacrylate glue and, if not already present, a headplate was attached. For electrophysiology experiments, a small craniotomy was performed (approximately 0.3 mm in diameter) guided by the activity maps of the visual cortex obtained by intrinsic optical imaging. After the recording, the mouse was either perfused for histology or its skull was protected with Kwik-Cast (World Precision Instruments) for the next experiment. For anatomical experiments, the skin was sutured after the viral injection using 6–0 suture silk (Fisher Scientific NC9134710). To reverse the anesthesia induced by the Fentanyl-Midazolam-Dexmedetomidine mixture, a mixture of Naloxone (Hospira, 1.2 mg/kg), Flumazenil (West-Ward Pharmaceuticals, 0.5 mg/kg), and Atipamezol (Zoetis, 2.5 mg/kg) was injected subcutaneously after the surgical procedures.

Visual stimulation.

Visual stimuli were generated using the open-source Psychophysics Toolbox[38] based on Matlab (MathWorks). Stimuli were presented at a distance of 15 cm to the left eye on a gamma-corrected LED-backlit LCD monitor (DELL) with a mean luminance of 20 cd/m^2. For two-photon experiments using a resonant scanner, the power source of the monitor's LED backlight was synchronized to the resonant scanner turnaround points (when data were not acquired) to minimize light leak from the monitor[39]. We presented drifting sinusoidal gratings (2 Hz, 0.04 cycles/°, 100% contrast) unless stated otherwise. The trial structure of all stimulus sessions (receptive field mapping, size tuning, …) was block randomized (the block size was given by the total number of parameter combinations). In all raster plots (Fig. 3, Fig. 5, and Extended Data Fig. 7), we separated stimulus conditions for clarity.

Intrinsic imaging: To estimate the visual area locations and their retinotopic maps using intrinsic imaging, we presented a narrow white bar (5°) on a black background, slowly drifting (10°/s) in one of the cardinal directions (10 to 20 trials per direction). In addition, we presented 25° patches of gratings at different retinotopic locations (usually one nasal and one temporal, 20 trials each). Gratings were presented for 2 s at 8 different directions (0.25 s each) followed by 13 s of gray screen.

Receptive field mapping: Stimuli consisted of either a 20° circular grating patch on a gray screen (classical stimulus) or a 20° gray circular patch on a full-field grating (i.e. large gratings covering the entire screen, approximately 120 × 90°; inverse stimulus) with a 15° spacing between the center of the patches (regular grid). For two-photon calcium imaging experiments, stimuli were presented for 1 s at a single direction or for 2 s at the four cardinal directions (0.5 s each). Stimulation periods were interleaved by 2 s of gray screen. We recorded 5 to 10 trials per stimulus condition. For electrophysiological experiments, stimuli were presented for 0.5 s at a single direction interleaved by 1 s of gray screen. We recorded 20 trials per stimulus condition. In addition, we used a finer grid of grating patches in a subset of experiments (patches of 10° with a spacing of 5°; Extended Data Fig. 4a, b).

Orientation tuning: We presented gratings of at least 15° diameter drifting in 8 directions (5 to 10 trials and 20 trials per direction for two-photon calcium imaging and electrophysiology experiments, respectively). For Extended Data Fig. 3, we additionally presented inverse gratings drifting in 8 directions, centered on the classical feedforward receptive field (ffRF). Stimulus presentation time was 1 s interleaved with 1.5 to 2 s of gray screen.

Size tuning: Patches of gratings and inverse gratings were displayed at 9 different sizes, equally spaced from 5 to 85° in diameter (10 trials per size; for two-photon experiments) or at 5 different sizes, equally spaced from 5 to 45° in diameter (20 to 30 trials per size; for electrophysiology experiments), centered on the ffRF. Stimulation time was either 2 s interleaved by 4 s of gray screen (for two-photon experiments) or 1 s interleaved by 1.5 s of gray screen (for electrophysiology experiments). Trials with optogenetic stimulation had an additional 1 s pre-stimulus and 0.5 s post-stimulus gray screen during which the optogenetic light source was turned on and the total number of trials was doubled (Optogenetics below). In addition, we blurred the edge of the patches using a sigmoid function rising from 1% to 99% over 10° in a subset of experiments (Extended Data Fig. 1). All other parameters were the same as for the size tuning described above.

Contrast tuning: We simultaneously presented classical and inverse stimuli with several test contrasts (0, 2^{-6}, 2^{-5}, …, 1). Stimuli were presented for 2 s interleaved by 4 s of gray screen (10 trials per stimulus combination).

Response dynamics: To estimate the temporal response profile to inverse stimuli (Fig. 3), we presented patches of gratings and inverse gratings at a single size (1000 trials each). These gratings were presented either at 15° or 20°, for 0.5 s interleaved by 1 s of gray screen. The initial phase of the drifting gratings was randomized to avoid overestimating the onset delay of the response for simple-cell-like receptive fields.

Behavioral monitoring.

All mice were habituated (3 to 5 days) to experimental rigs before starting experiments. During all awake experiments, we recorded the positions of the left eye using a CMOS camera (DMK23UM021, Imaging Source) with a 50 mm lens (M5018-MP, Moritex), tracked the running speed of the mouse, and monitored its general behavior using a webcam

(LifeCam Cinema 720p HD, Microsoft). Excluding eye-movement or running trials did not affect the results. For experiments under anesthesia that followed awake experiments (Fig. 4 and Extended Data Fig. 6), mice were anesthetized with isoflurane (approximately 1% in O_2) delivered with a nose cone. After induction of anesthesia, mice's body temperature was monitored and kept constant. To ensure an adequate depth of anesthesia, we tracked the left eye and monitored general behavior.

Intrinsic optical imaging.

We used intrinsic optical imaging to identify the center of primary visual cortex (V1) or the locations of HVAs. We sedated the mice with chlorprothixene (0.7 mg/kg) then lightly anesthetized with isoflurane (0.5 to 1% in O_2) delivered through a nose cone. The rectal temperature was monitored and maintained at 37°C. We illuminated visual cortex with 625 nm light from two LED light sources (M625F2, Thorlabs) using 1.5 mm light fibers (FP1500URT, Thorlabs). The intrinsic optical signal was measured with an Olympus MVX stereo-macroscope using a narrow bandpass filter (700/13 nm BrightLine, Semrock). We acquired the images at 10 Hz with a CCD camera (Orca-Flash 4.0 v2, Hamamatsu) using custom-written software in LabVIEW (National Instruments).

Two-photon calcium imaging.

Imaging was performed using either a galvanometric-scanner based MOM (Sutter) or a resonant-scanner based (8 kHz) Bergamo II two-photon microscope (Thorlabs), both controlled by ScanImage (Vidrio). Using the MOM system, we acquired images of 128 × 128 pixels at a single depth at 5.92 Hz frame rate. With the Bergamo II, we acquired images of 380 × 512 pixels at 1 or 4 depths at 40 Hz or 8 Hz frame rate, respectively. We obtained similar results with both systems, so all data were pooled. The illumination light source was a Ti:sapphire laser (Chameleon Ultra II, Coherent) used at an excitation wavelength of 910 nm for green indicator imaging and of 1040 nm for red indicator imaging. The laser power under the objective (16×, Nikon) never exceeded 50 mW (laser pulse width 140 fs at a repetition rate of 80 MHz).

Electrophysiology.

We performed extracellular recordings using multi-electrode silicon probes (A1×32-Edge-5mm-20–177-A32, NeuroNexus) with 32 channels spaced by 20 μm. The recording electrodes were controlled with micromanipulators (Luigs&Neumann) and coated with DiO lipophilic dyes (Life Technologies) for *post hoc* identification of the electrode track. We recorded the bandpass-filtered (0.1 Hz to 7.5 kHz) signals at 30 kHz using an Intan system (RHD2000 USB Interface Board, Intan Technologies).

Optogenetics.

We used the VGAT-ChR2-EYFP mouse line to ensure a homogeneous expression of the opsin. To silence parts of visual cortex, we used a 473 nm laser (LuxX 473–80, Omicron-Laserage). The light was first guided through a pinhole to collimate the beam, then sent through a long-range focal lens (AC254–300-A, Thorlabs) to focus the light onto the cortical surface (theoretical spot size ≤ 200 μm), before it entered a 2D-galvo system (GVS202,

Thorlabs) to direct the light to the regions of interest. The scanners were controlled by custom-written software in LabVIEW (National Instruments) and guided by a CMOS camera (DMK23UM021, Imaging Source) with a 50 mm lens (M5018-MP, Moritex). For Fig. 5a–e and Extended Data Fig. 7–9, we defined 8 HVAs (P, LI, LM, AL, RL, AM, PM, and M) based on the intrinsic optical imaging maps established before the optogenetic experiment (see Data analysis, Intrinsic optical imaging maps). These areas were consecutively scanned in a circular manner with a dwell time of ≤ 1 ms per area (resulting in 125 Hz frequency for the whole cycle). The laser was briefly shut off each time the beam moved from area M and P to avoid silencing parts of V1 (see Visual Stimulation for timing within a trial). For assessing the role of single HVAs in the generation of inverse tuning, we targeted each area individually (Extended Data Fig. 9). To verify the effectiveness of the silencing using this approach, we performed control recordings by scanning over the recording site in V1 (Extended Data Fig. 7a–c). To measure the spatial extent of silencing, we parked the laser at 5 locations at and around the recording site (800 μm and 400 μm lateral and medial of the recording site and on the recording site itself, randomizing which location to silence for each trial), targeted individual HVAs, or scanned over these 8 HVAs (Extended Data Fig. 7d–g). For experiments scanning over all 8 HVAs, the laser power was set to approximately 0.75 mW/mm^2 (total power at the surface of cortex was 3 mW distributed over approximately 4 mm^2 of illuminated HVAs). For experiments targeting individual locations or HVAs, the laser power was set to approximately 4 mW/mm^2 (total power at the surface of cortex: 2 mW).

Histology.

Mice were deeply anesthetized with 5% isoflurane and urethane, and transcardially perfused with PBS followed by 4% paraformaldehyde in PBS. The brain was then embedded in 2 to 3% agar and 100 μm thick sections were cut using a microtome (Leica VT1000 S vibratome). Slices were mounted using a Vectashield HardSet mounting medium containing DAPI (H-1500–10, Vector Laboratories H1500). Images were acquired with an Olympus MVX10 MacroView microscope or a Nikon Ti CSU-W1 inverted spinning disk confocal microscope, and analyzed with Fiji[40].

For electrophysiology experiments, the penetration depth was estimated *post hoc* using the DiO track of the electrode (see Electrophysiology) and the layer 4/layer 5 border was defined based on the DAPI staining. This allowed us to determine which pins of the electrode were located in layer 5/6 (L5/6). For scatter plots, inverse-tuned units (see Data analysis) were defined as L2/3 or L5/6 units if they were above or below this border, respectively.

To identify and quantify inhibitory long-range projections from HVAs to V1 (Extended Data Fig. 7h–l), we injected an AAVretro.CAG.Flex.tdTomato in V1 of GADcre mice and waited approximately 3 weeks before sacrificing the mice. The borders between V1 and the HVAs were defined based on the DAPI staining using the thickness of L4. Based on these borders and a mouse atlas[41], we defined the location and identity of HVAs. To quantify the number of inhibitory neurons in HVAs projecting to V1, we counted the tdTomato-positive cell

bodies in the coronal slice that contained the center of the area. Note that this underestimates the difference in the number of projection neurons between V1 and HVAs.

Data analysis.

All data were analyzed using custom-written code in Matlab (MathWorks).

Two-photon calcium imaging: We analyzed two-photon calcium imaging data as described previously[42]. Briefly, data were full-frame registered using custom-written software (https://sourceforge.net/projects/iris-scanning/). We selected the neurons semi-manually, based on mean and maximum projection images. We calculated the raw fluorescence traces as the average fluorescence of all pixels within a selected region of interest for each frame. Fluorescence changes (ΔF/F) were calculated as described elsewhere[43]. All stimulus evoked responses were baseline subtracted (1 s pre-stimulus interval).

Extracellular recordings: We determined single unit firing using KiloSort and Phy (https://github.com/cortex-lab/KiloSort). We determined the spike times with 1 ms resolution. Inhibitory units were defined as units that significantly increased their firing rate during optogenetic stimulation in the absence of a visual stimulus, i.e. during the pre-visual-stimulus baseline. All stimulus evoked responses were baseline subtracted (0.5 s pre-stimulus interval).

Response amplitude: The response amplitude to a stimulus was computed as the average response over the duration of the stimulus presentation (excluding the first 0.5 s of each trial for two-photon experiments due to the delay and slow rise of calcium indicators). Responses were normalized by the maximum response over the relevant stimulus parameter space and then averaged over neurons or units. We defined significant responses as responses that exceeded a z-score of 3.29 (corresponding to $p < 10^{-3}$) or 5.33 (corresponding to $p < 10^{-7}$; for two-photon experiments in L4).

Receptive field mapping: To estimate the center of the receptive field, we fitted the responses to patches of gratings with a two-dimensional Gaussian. We excluded neurons if they failed to have at least one significant trial-averaged response within 10° of their estimated centers (or the closest data point if no stimulus was located within 10°). For the comparison of the average receptive field maps to classical and inverse stimuli (Fig. 1 and 2, Extended Data Fig. 4 and 5), we only included neurons with at least one significant average response to a classical and an inverse stimulus at any location. To compare regular and fine receptive field mapping (Extended Data Fig. 4), neurons were only included if they responded to both fine and regular grid stimuli and if their estimated receptive field center (of the regular grid) was within the surface covered by the fine mapping stimuli (see smaller dashed rectangle in Extended Data Fig. 4a). To illustrate the average receptive fields (heat maps in Fig. 1, Extended Data Fig. 4 and 5), we used a spline interpolation and smoothed the overall average with a two-dimensional Gaussian filter (10°). We excluded neurons from further analysis (e.g. size tuning, …) if the estimated centers of their ffRFs were not within 10° of the centers of the stimuli presented to establish size tuning, orientation tuning, (…).

Size tuning: We fitted the data to an integral over a difference of Gaussians. This fit was used to estimate the neurons' ffRF and feedback receptive field (fbRF) sizes. We approximated the ffRF size by the size of the patch of gratings evoking the largest response (size tuning fits were bound to the interval 0.1 to 90.1°). Note that we excluded neurons from further analysis if they failed to respond to at least one classical stimulus of any size. To compare size tuning with sharp and burred edges, neurons had to respond to at least one classical stimulus of any size for both stimulus types (sharp and blurred; Extended Data Fig. 1). Surround suppressed neurons were defined as neurons in which the responses to any classical stimulus were significantly larger than those to the largest classical stimulus tested (Extended Data Fig. 5). We calculated the suppression index as the average response over the two largest stimuli presented divided by the maximum response (Extended Data Fig. 8c). The same sizes were used to calculate the suppression index during HVA silencing.

Defining inverse-tuned neurons: Neurons were defined as inverse tuned if they significantly responded to at least one classical and one inverse stimulus and if their response to at least one inverse stimulus of any size centered on their ffRF was significantly larger than that to a full-field stimulus (or approximated by the response to the largest classical or smallest inverse stimulus presented).

Inverse tuning index (ITI): We defined the inverse tuning index as:

$$ITI = \frac{R_{inv} - R_{cla}}{2 \times ((R_{inv} - R_{ff}) + (R_{cla} - R_{ff}))} + 0.5$$

With R_{inv}: maximum response to inverse stimuli, R_{cla}: maximum response to classical stimuli, and R_{ff}: response to a full-field stimulus.

Orientation tuning: We fitted a circular sum of Gaussians with a peak offset of 180° and equal tuning width (full width at half maximum of the Gaussian fit). We calculated orientation selectivity index (OSI) and direction selectivity index (DSI) as described elsewhere[10]. Classical and inverse stimuli were presented at a fixed stimulus diameter (10°, 15°, or 20°). Neurons were excluded from this analysis (Extended Data Fig. 3b–g) if their classical and inverse preferred sizes were not within 10° of the presented stimulus size.

Contrast tuning: Classical and inverse stimuli were presented at a fixed stimulus diameter (10°, 15°, or 20°) and at one orientation. Neurons were excluded from this analysis (Extended Data Fig. 3h) if their classical and inverse preferred sizes were not within 10° of the presented stimulus size. Moreover, we excluded neurons if their OSIs were above and ≥ 0.3 AND if their orientation preference was not within 45° of the presented stimulus orientation. In other words, we excluded neurons that were strongly orientation tuned to the orthogonal orientation.

Response dynamics: To estimate the response delay, rise time, and onset slope for classical and inverse stimuli, we binned the spike times in bins of 10 ms and then median filtered (50 ms) the average traces. We defined the response delay as the first data point after stimulus onset that crossed a z-score threshold of 5.33 (corresponding to $p < 10^{-7}$). Further,

we defined the rise time as the interval between the response onset (as estimated for the response delay) and the first time point crossing 75% of the maximum response during stimulus presentation (changing this arbitrary value to 50% or 100% did not affect the results). Finally, we estimated the response onset slope as the fitted slope to the response during the initial rise time. We excluded units whose responses did not exceed the response threshold defined above. Furthermore, for the population responding to the classical stimulus (Fig. 3g), units were excluded if their preferred classical size was larger than the presented stimulus size (±10°). For the inverse-tuned population (Fig. 3g), units were excluded if their preferred inverse size was smaller than the presented size (±10°). For the inverse-tuned subpopulation of units responding to both (Fig. 3c–f), both classical and inverse sizes were required to be within 10° of the presented stimulus size.

Awake/anesthetized: Neurons were included in this analysis based on their awake responses (Fig. 4 and Extended Data Fig. 6). However, to ensure that the stimuli were also centered on the receptive fields under anesthesia, neurons were excluded if the estimated centers of their ffRFs under anesthesia were not within 10° of the centers of the anesthetized size tuning stimuli presented. To estimate the peak response of a neuron under anesthesia, we used the same size as in the awake condition (±10°).

Size tuning of (non-centered) LM boutons to stimuli centered on their putative V1 targets: Size tuning stimuli were presented at a location such that the population-averaged center of the V1 receptive fields was within 10° (Extended Data Fig. 10f, left). LM boutons were excluded from this analysis if they failed to respond to any size tuning stimulus of any size (classical or inverse) and if their estimated centers of their ffRFs were within 10° of the centers of the presented size stimuli (Extended Data Fig. 10h). Hence, only putative offset boutons were included. Additionally, for Fig. 5i, boutons needed to respond to an inverse stimulus of any size (stimulus was NOT centered on the boutons' receptive fields).

Intrinsic optical imaging maps: We calculated the temporal phase of the Fourier component at the frequency of the bar presentation. This gave us the complete extent of V1. For locating HVAs, we cross checked the Fourier maps with those obtained from the responses to patches of gratings at different retinotopic locations and confirmed them by standard maps in the literature[44].

Modulation index: We calculated the modulation indexes as the difference between the activity during the optogenetic and the control condition divided by the sum of the two.

Inclusion criteria: For significant thresholds and other details, see above.

Fig. 1b: As mentioned above, we estimated the center of the receptive field by fitting the responses to patches of gratings presented along a grid with a two-dimensional Gaussian. Neurons were included if they significantly responded to patches of gratings at any location within 10° of their estimated centers, and they significantly responded to at least one inverse stimulus at any location.

Fig. 1c: We estimated the center of the receptive field by fitting the responses to patches of gratings presented along a grid with a two-dimensional Gaussian. Neurons were included if they significantly responded to patches of gratings at any location within 10° of their estimated centers, their estimated centers were within 10° of the center of the size tuning stimuli, and they significantly responded to at least one classical size tuning stimulus.

Fig. 1e, f: Same criteria as for Fig. 1b, c, respectively.

Fig. 2: Receptive field maps and size-tuning functions, same criteria as for Fig. 1b, c, respectively.

Fig. 3b–f: We estimated the center of the receptive field by fitting the responses to patches of gratings presented along a grid with a two-dimensional Gaussian. Units were included if they significantly responded to patches of gratings at any location within 10° of their estimated centers, their estimated centers were within 10° of the center of both the classical and inverse stimuli presented to assess the response dynamics (response dynamics stimuli), they were inverse tuned, both their classical and inverse preferred sizes were within 10° of the size of the response dynamics stimuli, and they significantly responded to both classical and inverse response dynamics stimuli.

Fig. 3g: Units were included for which the criteria used for 3b-f apply for either the classical or the inverse stimulus, but not necessarily for both. Classical - We estimated the center of the receptive field by fitting the responses to patches of gratings presented along a grid with a two-dimensional Gaussian. Units were included if they significantly responded to patches of gratings at any location within 10° of their estimated centers, their estimated centers were within 10° of the center of the classical stimuli presented to assess the response dynamics (classical response dynamics stimuli), their classical preferred sizes were within 10° or less than the size of the classical response dynamics stimuli, and they significantly responded to the classical response dynamics stimuli. Inverse - We estimated the center of the receptive field by fitting the responses to patches of gratings presented along a grid with a two-dimensional Gaussian. Units were included if they significantly responded to patches of gratings at any location within 10° of their estimated centers, their estimated centers were within 10° of the center of the inverse response dynamics stimuli, their inverse preferred sizes were within 10° or more than the size of the inverse response dynamics stimuli, and they significantly responded to the inverse response dynamics stimuli.

Fig. 4: We estimated the center of the receptive field by fitting the responses to patches of gratings presented along a grid with a two-dimensional Gaussian. Neurons were included if they significantly responded to patches of gratings at any location within 10° of their estimated centers (awake and anesthetized), their estimated centers were within 10° of the center of the size tuning stimuli (awake and anesthetized), and they significantly responded to at least one classical size tuning stimulus (only awake).

Fig. 5c–e: We estimated the center of the receptive field by fitting the responses to patches of gratings presented along a grid with a two-dimensional Gaussian. Units were included if they significantly responded to patches of gratings at any location within 10° of their estimated centers, their estimated centers were within 10° of the center of the size tuning

stimuli, they significantly responded to at least one classical size tuning stimulus, and they were inverse tuned.

Fig. 5g: Same criteria as for Fig. 1c.

Fig. 5i: We estimated the center of the receptive field by fitting the responses to patches of gratings presented along a grid with a two-dimensional Gaussian. Boutons were included if they did not significantly respond to patches of gratings at any location within 10° of their estimated centers or if their estimated centers were not within 10° of the center of the size tuning stimuli, and if they significantly responded to at least one inverse size tuning stimulus.

Statistics.

We used Wilcoxon rank-sum tests for independent group comparisons, Wilcoxon signed-rank tests for paired tests and Student's t-tests for a single group analysis. No statistical methods were used to pre-determine sample sizes, but our sample sizes were similar to those used in previous publications. Allocation into experimental groups was not randomized. Data collection and analysis were not preformed blind to the experimental conditions.

Extended Data

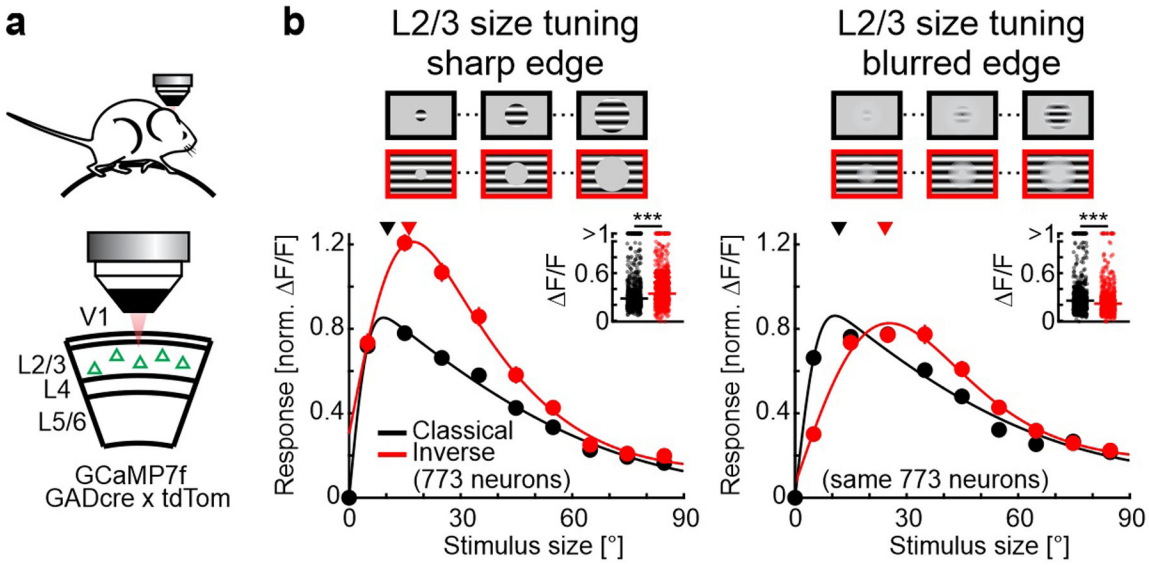

Extended Data Figure 1 |. Robust responses to inverse stimuli with blurred edges.

a, Experimental configuration. **b**, Top: Schematic of stimuli used for size-tuning functions. Bottom: Population-averaged size tuning of classical and inverse stimuli with sharp edges (left) and stimuli with blurred edges (right; see Methods). Here and in all other figures, black and red traces are responses to classical and inverse stimuli, respectively, and shaded areas are periods of stimulus presentation. Solid lines are fits to the data (see Methods). Triangles above size-tuning functions indicate median preferred size for each condition. Insets: Maximum responses. Horizontal lines, medians. Two-sided Wilcoxon signed-rank test; sharp edge, ***: $p = 2.0 \times 10^{-9}$; blurred edge, ***: $p = 4.5 \times 10^{-10}$; 773 neurons in 4 mice. Traces

and data points represent mean ± SEM (shading or error bars, respectively). Here and in all other figures, error bars are present but sometimes smaller than symbols.

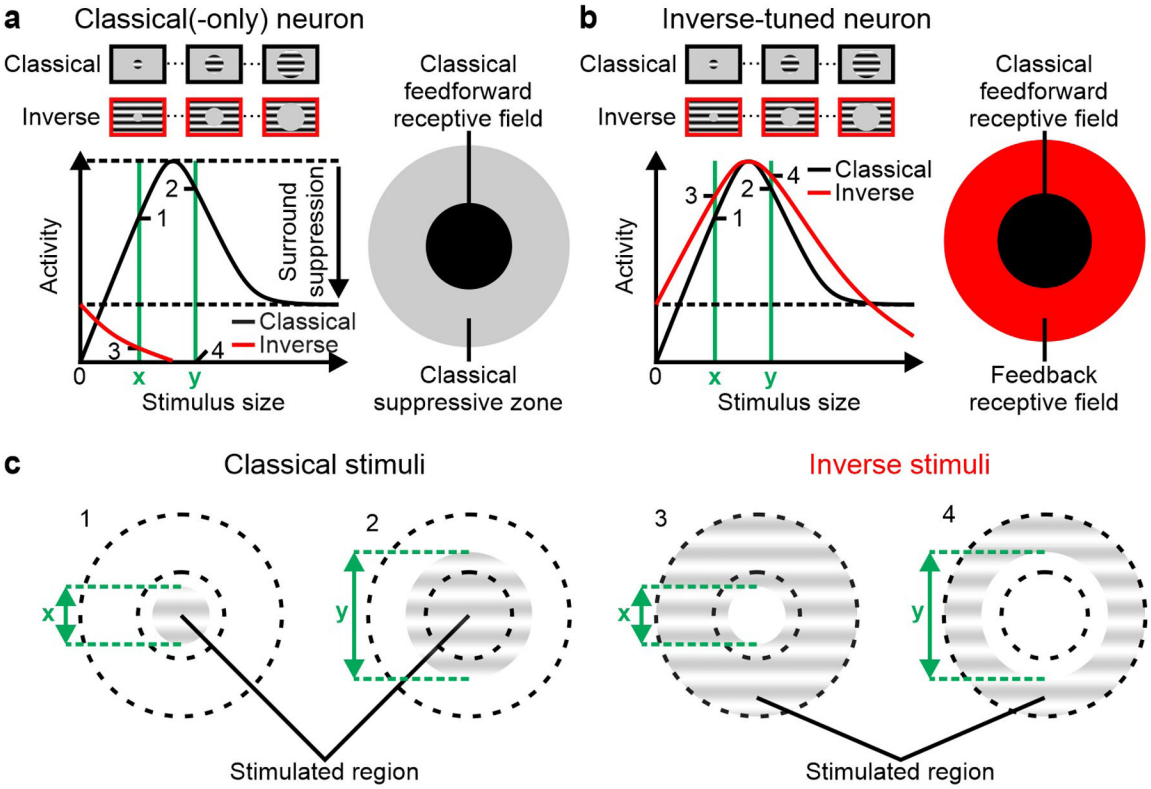

Extended Data Figure 2 |. Illustration of classical and inverse-tuned neurons.

a, Classical(-only) neuron. Left: The response of a neuron probed with classical stimuli (black) increases with the size of the stimulus until it peaks at the neuron's preferred size (top horizontal dotted line). The response then decreases due to surround suppression (maximum suppressed level indicated by the lower dotted horizontal line). The response of the same neuron probed with inverse stimuli (red) starts at the maximally surround suppressed activity level (an inverse stimulus with a size of 0° is a full-field grating) and then decreases as the diameter of the gray patch increases, consistent with visual stimulation being progressively removed from the classical feedforward receptive field (ffRF). Right: Schematic of a neuron's ffRF surrounded by its classical suppressive zone. **b**, Inverse-tuned neuron. Left: The response of the neuron probed with inverse stimuli (red) starts, as for the classical-only neuron, at the maximally surround suppressed activity level but then it increases until reaching the neuron's preferred inverse stimulus size and decreases with larger diameters of the gray patch consistent with visual stimulation being progressively removed from the feedback receptive field (fbRF). Right: Schematic of a neuron's ffRF surrounded by its fbRF. **c**, Four example stimuli: Two classical stimuli (1 and 2 of sizes x and y, respectively) and two inverse stimuli (3 and 4, also of sizes x and y, respectively). The inner dotted circle represents the outer border of the classical ffRF. The outer dotted circle represents the outer border of the suppressive region and, for inverse-tuned neurons, also the outer border of the fbRF. The response amplitudes to the four example stimuli (1 to 4) in a

classical-only neuron and in an inverse-tuned neuron, are marked in (**a**) and (**b**), respectively, at the intersection between the green vertical lines (stimulus size) and the size-tuning functions.

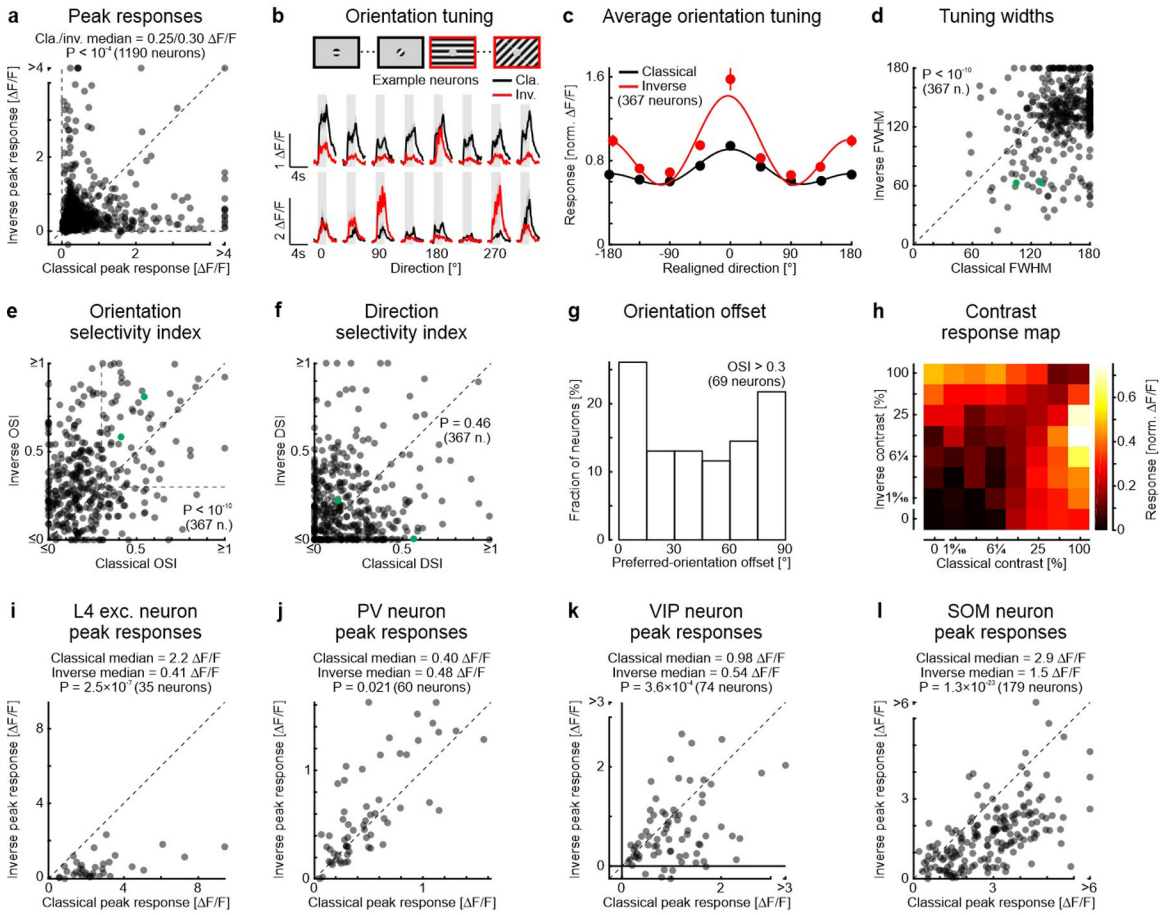

Extended Data Figure 3 |. Classical and inverse tuning properties in layer 2/3 excitatory neurons. **a**, Scatter plot of L2/3 excitatory neuron peak responses (maximum responses to size tuning curves in Fig. 1c) of inverse-tuned neurons to classical and inverse stimuli. Classical and inverse median, 0.25 and 0.30 ΔF/F, respectively. Two-sided Wilcoxon signed-rank test; p = 7.7×10^{-5}; same excitatory layer 2/3 (L2/3) neurons as in Fig. 1c; 1190 neurons in 9 mice. **b**, Top: Schematic of stimuli presented at different orientations to map the classical and inverse orientation preferences. We tested 8 orientations at intervals of 45° at the neuron's preferred stimulus size and location using either a classical or an inverse stimulus. Bottom: Calcium responses of two example neurons in primary visual cortex (V1) for each orientation using classical and inverse stimuli. **c**, Population-averaged tuning curve for classical and inverse stimuli. Each neuron's preferred orientations (independently for classical and inverse stimuli) were aligned to 0° and its activity normalized to its maximum response (367 neurons in 4 mice). Solid lines are fits to the data (see Methods). **d**, Tuning widths of orientation tuning curves obtained with classical stimuli compared to those obtained with inverse stimuli. For each neuron, tuning width was defined as the full width at half maximum (FWHM) of the fitted tuning curve. Two-sided Wilcoxon signed-rank test; p

= 1.8 × 10^{-21}; 367 neurons in 4 mice. Green symbols represent the example neurons shown in (**b**). **e**, Same for orientation selectivity indexes. The horizontal and vertical lines at 0.3 delimit the orientation-selective population. Two-sided Wilcoxon signed-rank test; p = 7.0 × 10^{-16}; 367 neurons in 4 mice. **f**, Same for direction selectivity indexes. Two-sided Wilcoxon signed-rank test; p = 0.46; 367 neurons in 4 mice. **g**, Distribution of orientation offsets. For orientation-selective neurons only (see (**e**), with both OSIs ≥ 0.3), an orientation offset was computed, defined as the absolute difference in orientation between a neuron's preferred orientation for a classical and an inverse stimulus. **h**, Contrast response map. Classical and inverse stimuli were presented simultaneously, and different combinations of contrasts were tested. The contrast heat map was obtained by averaging normalized activity (86 neurons in 4 mice). Traces and data points represent mean ± SEM (shading or error bars, respectively). **i**, Scatter plot of L4 neuron peak responses (maximum responses to size tuning curves in Fig. 1f) of inverse-tuned neurons to classical and inverse stimuli. Classical and inverse median, 2.2 and 0.41 ΔF/F, respectively. Two-sided Wilcoxon signed-rank test; p = 2.5 × 10^{-7}; same layer 4 (L4) neurons as in Fig. 1f; 35 neurons in 6 mice. **j**, Scatter plot of PV neuron peak responses of inverse-tuned neurons to classical and inverse stimuli. Classical and inverse median, 0.40 and 0.48 ΔF/F, respectively. Two-sided Wilcoxon signed-rank test; p = 0.021; same PV neurons as in Fig. 2b, bottom; 60 neurons in 7 mice. **k**, Scatter plot of VIP neuron peak responses of inverse-tuned neurons to classical and inverse stimuli. Classical and inverse median, 0.98 and 0.54 ΔF/F, respectively. Two-sided Wilcoxon signed-rank test; p = 3.6 × 10^{-4}; same VIP neurons as in Fig. 2c, bottom; 74 neurons in 8 mice. **l**, Scatter plot of SOM neuron peak responses of inverse-tuned neurons to classical and inverse stimuli. Classical and inverse median, 2.9 and 1.5 ΔF/F, respectively. Two-sided Wilcoxon signed-rank test; p = 1.3 × 10^{-23}; same SOM neurons as in Fig. 2d, bottom; 179 neurons in 5 mice.

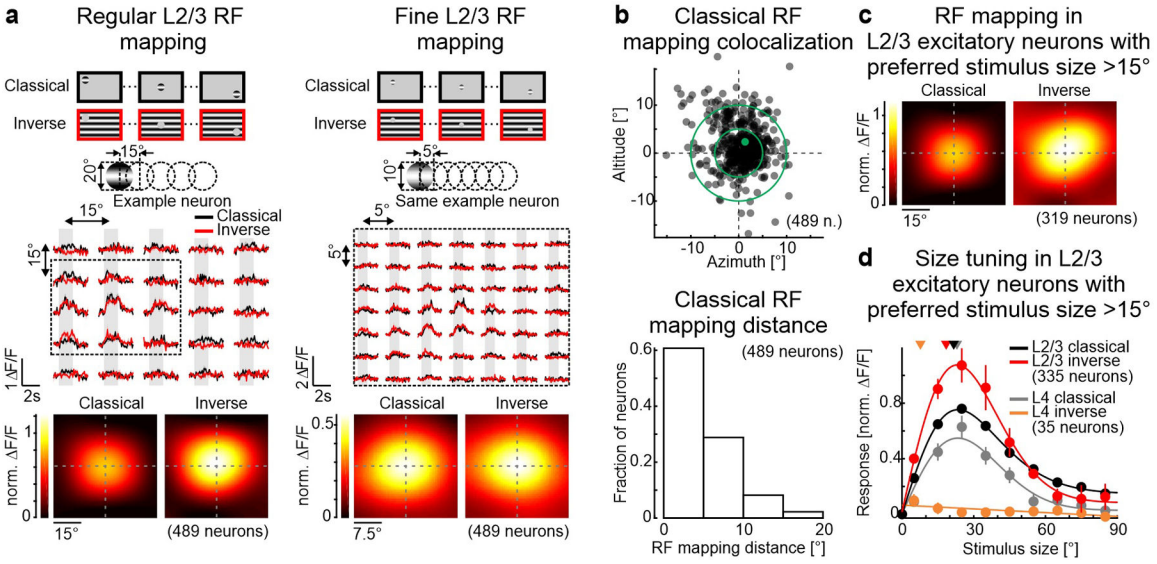

Extended Data Figure 4 |. Inverse tuning is not due to low mapping resolution.

a, Top left: Schematic of regular receptive field mapping. Stimulus diameter of 20° with a grid spacing of 15°. Center left: Trial-averaged calcium responses from an example neuron

for each stimulus location. Bottom left: Population-averaged receptive field for responses to classical or inverse stimuli aligned to the center of the ffRF (489 neurons in 4 mice). Right: Same but with fine receptive field mapping. Stimulus diameter of 10° with a grid spacing of 5° (only for part of the visual space covered with the regular mapping, see dotted rectangle on the left). **b**, Top: Spatial offset of regular ffRF mapping compared to fine ffRF mapping (same 489 neurons in 4 mice). For each neuron, its ffRF center estimated by the fine grid mapping is aligned at [0,0] and the localization of its estimated ffRF center estimated by the regular grid is plotted with respect to the fine grid estimated center. Bottom: Distribution of distances between the center of ffRF estimated by fine grid mapping and the center estimated by regular grid mapping (approximately 90% of neurons have a distance between the two centers below 10°). Green symbol represents the example neuron shown in (**a**). **c**, Population-averaged receptive field for responses to classical or inverse stimuli aligned to the center of the ffRF and only for L2/3 neurons that had a preferred ffRF size of more than 15° (319 neurons in 9 mice). **d**, Population-averaged size-tuning functions for classical (black: L2/3 neurons with ffRF > 15°, 335 neurons in 9 mice; gray: L4 neurons, 35 neurons in 6 mice) and inverse (red: L2/3 neurons with ffRF > 15°, 335 neurons in 9 mice; orange: L4 neurons, 35 neurons in 6 mice) stimuli. Solid lines are fits to the data (see Methods). Triangles above size-tuning functions indicate median preferred size for each condition. Inset: Maximum responses. Horizontal lines, medians. L2/3 neurons with ffRF size > 15°; Two-sided Wilcoxon signed-rank test; *: $p = 6.7 \times 10^{-3}$; 335 neurons in 9 mice. Traces and data points represent mean ± SEM (shading or error bars, respectively).

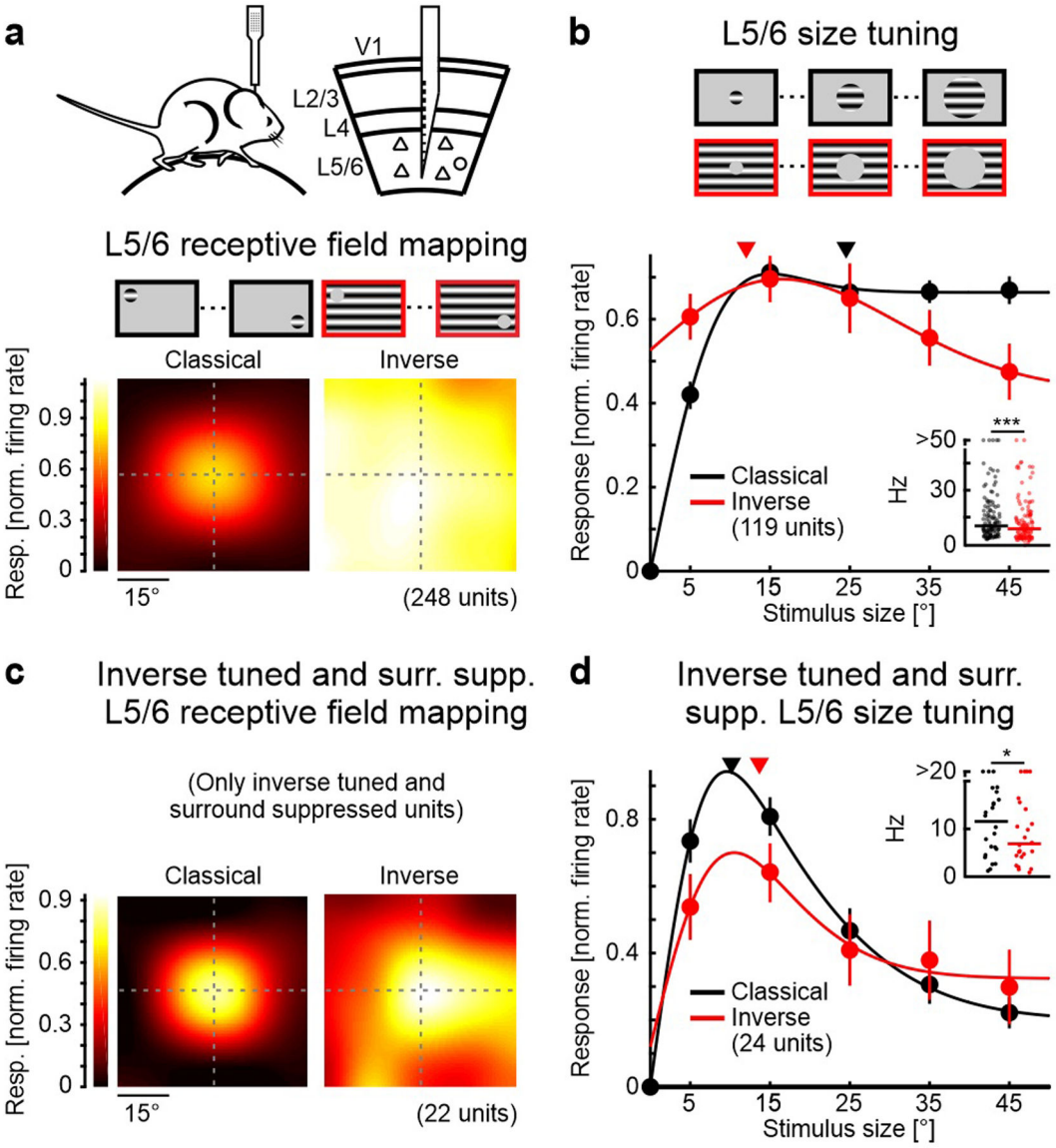

Extended Data Figure 5 |. Responses to inverse stimuli in layer 5/6.

a, Receptive field mapping of layer 5/6 (L5/6) neurons using classical and inverse stimuli. Top: Experimental configuration. Electrophysiological recordings were obtained in awake mice. The silicon probe spanned all layers, including deep layers (see Methods for layer definition). Center: Receptive fields were mapped using classical and inverse stimuli. Bottom left: Population-averaged ffRFs for L5/6 neurons. Bottom right: Same for inverse stimuli, aligned relative to the center of the ffRF (248 units in 20 mice). **b**, Size tuning of L5/6 neurons using classical and inverse stimuli. Top: Schematic of stimuli used for size-tuning functions. The classical and inverse stimuli were presented at the same location (within 10° of the estimated center of the ffRF). Bottom, normalized size-tuning functions for classical and inverse stimuli. Solid lines are fits to the data (see Methods). Triangles above size-tuning functions indicate median preferred size for each condition. Inset: Maximum responses. Horizontal lines, medians. Two-sided Wilcoxon signed-rank test; ***:

p = 1.1 × 10^{-4}; 119 units in 20 mice. **c** and **d**, same as (**a** and **b**) but for subset of L5/6 units defined both as surround suppressed and inverse tuned (as compared to (**b**) where all L5/6 units that responded to at least one classical stimulus size were included; see Methods) (**c**), 22 units in 12 mice; (**d**), Two-sided Wilcoxon signed-rank test; *: p = 0.016; 24 units in 12 mice. Data points represent mean ± SEM (error bars).

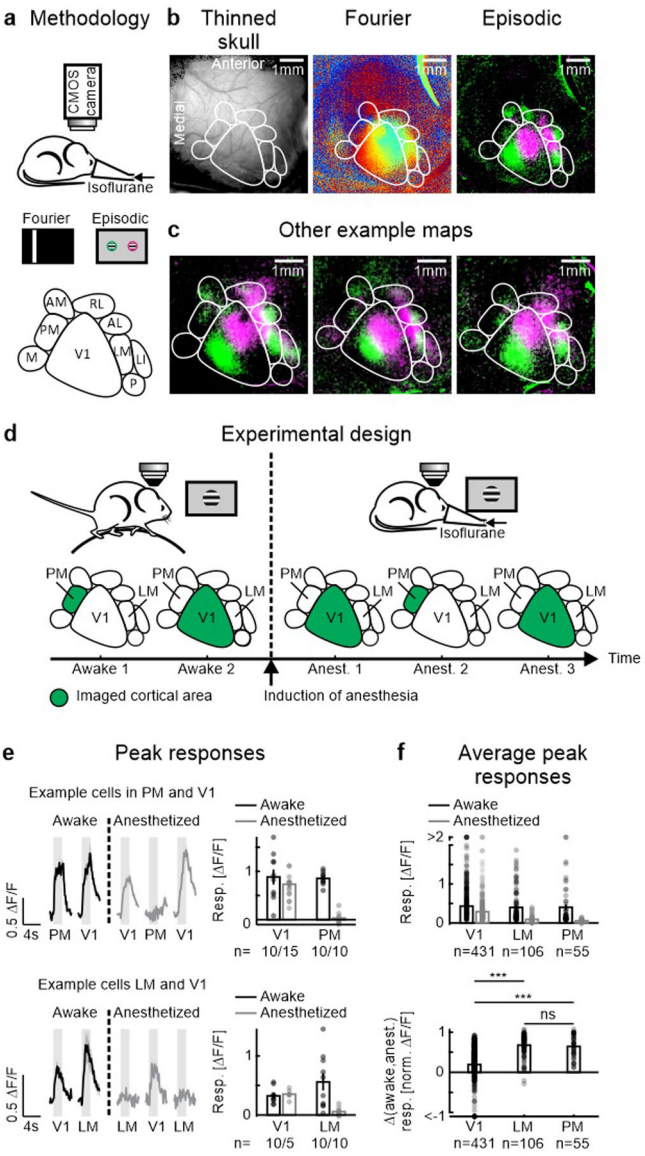

Extended Data Figure 6 |. Impact of anesthesia is more pronounced in higher visual areas.

a, Experimental configuration for intrinsic imaging of V1 and higher visual areas (HVAs). To estimate the visual area locations and their retinotopic maps using intrinsic imaging, we presented a narrow white bar (5°) on a black background, slowly drifting (10°/s) in one of the cardinal directions (“Fourier”). We calculated the temporal phase of the Fourier component at the frequency of the bar presentation. This gave us the complete extent of V1. For locating HVAs, we cross checked the Fourier maps with those obtained from the

responses to 25° patches of gratings at different retinotopic locations (“episodic”). **b**, Left: Blood vessel pattern visible through thinned skull. Center: Fourier map of same field of view obtained with a vertical var moving from nasal to temporal. Right: Episodic map of same field of view. Scale bar, 1 mm. **c**, Other example episodic maps. Scale bar, 1 mm. **d**, Experimental design to assess impact of anesthesia on V1 and HVAs. The responses to classical stimuli of neurons in a HVA, LM or PM, and V1 were recorded using two-photon calcium imaging. The experiment started in awake mice by imaging either a HVA or V1. After induction of anesthesia, the same neurons were imaged again. To reduce the influence of variability in anesthesia levels, the first imaged area under anesthesia was imaged again at the end of the experiment. **e**, Peak responses in visual areas. Top left: Example calcium response of a neuron located in PM and another neuron located in V1 in an awake mouse (black) and responses of the same neurons in the anesthetized mouse (gray). Top right: Trial-averaged peak response for the same neurons shown on the left for the awake (black) and anesthetized mouse (gray). Bottom, same for a different mouse but recorded in V1 and LM. **f**, Population-averaged peak responses in awake and anesthetized mice. Top: Population-averaged peak responses in V1, LM and PM for awake (black) and anesthetized mice (gray). Two-sided Wilcoxon signed-rank test; V1, $p = 6.2 \times 10^{-40}$, 431 neurons in 5 mice; LM, $p = 9.9 \times 10^{-19}$, 106 neurons in 3 mice; PM, $p = 1.1 \times 10^{-10}$; 55 neurons in 2 mice. Bottom: Population-averaged difference between normalized neuronal activity for awake and anesthetized state. For each neuron, all responses were normalized by the peak activity in the awake state before computing the differences. Two-sided Wilcoxon rank-sum test; V1, 431 neurons in 5 mice; LM, 106 neurons in 3 mice; PM, 55 neurons in 2 mice. V1-LM, ***: $p = 1.2 \times 10^{-25}$; V1-PM, ***: $p = 9.0 \times 10^{-13}$; LM-PM, ns: $p = 0.48$. Traces and bars represent mean ± SEM (shading or error bars, respectively).

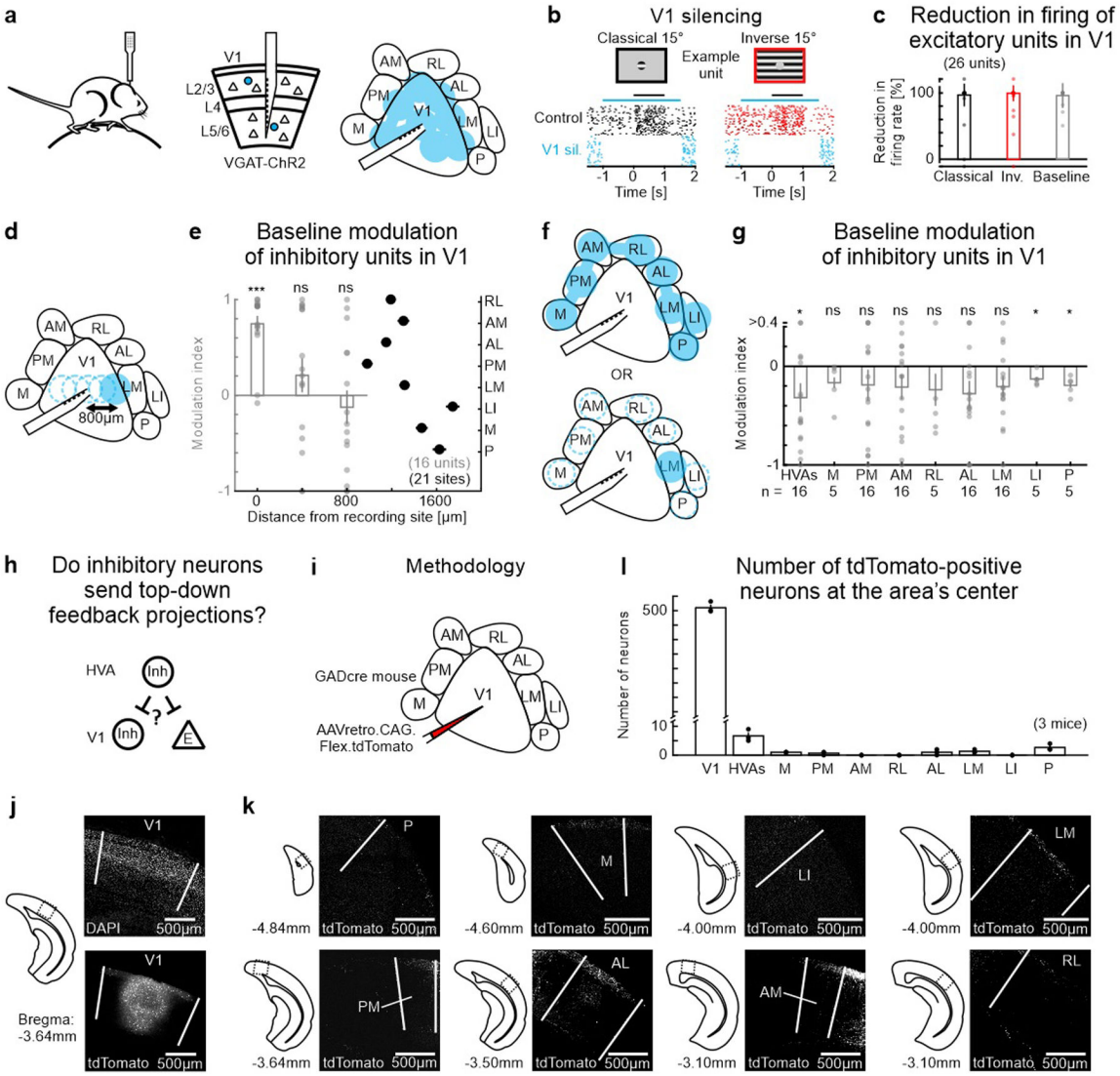

Extended Data Figure 7 |. Strong silencing by spatially restricted excitation of local inhibitory units.

a, Experimental configuration. A silicon probe was inserted in V1, spanning all cortical layers, in mice expressing Channelrhodopsin-2 in inhibitory neurons (VGAT-ChR2). To assess the strength of inhibition of excitatory units when using the laser scanning technique (Fig. 5; see Methods), the V1 recording site as well as seven other locations were scanned at 125 Hz. **b**, Raster plot of example excitatory unit in L5/6 in response to classical and inverse stimuli of 15° in diameter under control conditions (30 trials each) and during silencing of V1 (blue; V1 sil.). Black and blue horizontal lines are periods of stimulus presentation and V1 silencing, respectively. Classical and inverse stimuli were presented in random order; trials with V1 silencing were randomized as well but are separated here for clarity. **c**, Reduction in firing of excitatory units. The reduction in firing was measured as one minus the ratio between the optogenetic condition and the control condition. Note that silencing reached nearly 100% for both responses to classical and inverse stimuli, and for the baseline activity (26 units in 10 mice). **d**, Experimental configuration. To assess the effect of distance

on the optogenetic stimulation of inhibitory units at the recording site, two medial and two lateral locations at 400 μm and 800 μm from the V1 recording site were targeted for laser stimulation while recording in V1. **e**, Modulation of the baseline of inhibitory units. The modulation index was defined as the difference between the activity during the optogenetic and the control condition divided by the sum of the two. The modulation index was high at the recording site (at 0 μm) and quickly dropped with distance (gray bars; Two-sided Student's t-test; 0 μm, ***: $p = 2.0 \times 10^{-7}$; 400 μm, ns: p = 0.26; 800 μm, ns: p = 0.51; 16 units in 8 mice). As a comparison, the distance of the HVAs from the recording site is plotted on the same axis (black dots, right y-axis; 21 recording sites, 12 mice), suggesting that when pointing the laser at HVAs, direct activation of inhibitory neurons at the V1 recording site is unlikely. **f**, Experimental configurations. To assess the effect of the laser stimulation of HVAs on inhibitory units at the recording site, all 8 (top) or individual HVAs (bottom) were targeted for laser stimulation while recording in V1 (same configurations as during the experiments in Fig. 5 and Ext. Data Figs. 8 and 9). **g**, Modulation of the baseline of inhibitory units. The modulation indices were either negative or not significantly different from zero, indicating that the laser stimulation was unlikely to directly activate inhibitory neurons at the V1 recording site. Two-sided Student's t-test; HVA, *: p = 0.045; 16 units in 8 mice; M, ns: p = 0.16; 5 units in 4 mice; PM, ns: p = 0.24; 16 units in 8 mice; AM, ns: p = 0.11; 16 units in 8 mice; RL, ns: p = 0.46; 5 units in 4 mice; AL, ns: p = 0.051; 16 units in 8 mice; LM, ns: p = 0.064; 16 units in 8 mice; LI, *: p = 0.015; 5 units in 4 mice; P, *: p = 0.010; 5 units in 4 mice. **h**, Are there many inhibitory neurons projecting from HVAs to V1? **i,** Methodology. A retrograde virus, AAVretro.CAG.Flex.tdTomato, was injected in V1 of GADcre mice to label GAD-positive neurons projecting to the site of injection. **j**, Left: Outlines of the cortical section where the confocal images shown on the right were acquired. The location of the imaged area is further indicated by the dotted square depicted on the outline. Rostro-caudal distance to bregma is indicated below the outline. Right: Average intensity projection. Top right: DAPI staining highlights the higher density of neurons in layer 4 in V1 used to define V1 borders (white lines). Bottom: The tdTomato fluorescence reveals numerous cell bodies in V1 around the site of injection and even more distal in L1. **k**, Same as in (**j**) but only for the tdTomato fluorescence and for all HVAs targeted for laser stimulation in Fig. 5 and Ext. Data Figs. 8 and 9. White lines delimit area's boundaries. **l**, Quantification of tdTomato-positive neurons at the area's center. The number of tdTomato-positive neurons were counted in the section containing the center of the investigated area. "HVAs" represents the sum of tdTomato-positive neurons in all HVAs. Note the sparse inhibitory projections from HVAs to V1 but the abundance of local inhibitory projections within V1 (3 mice). Bars represent mean ± SEM (error bars).

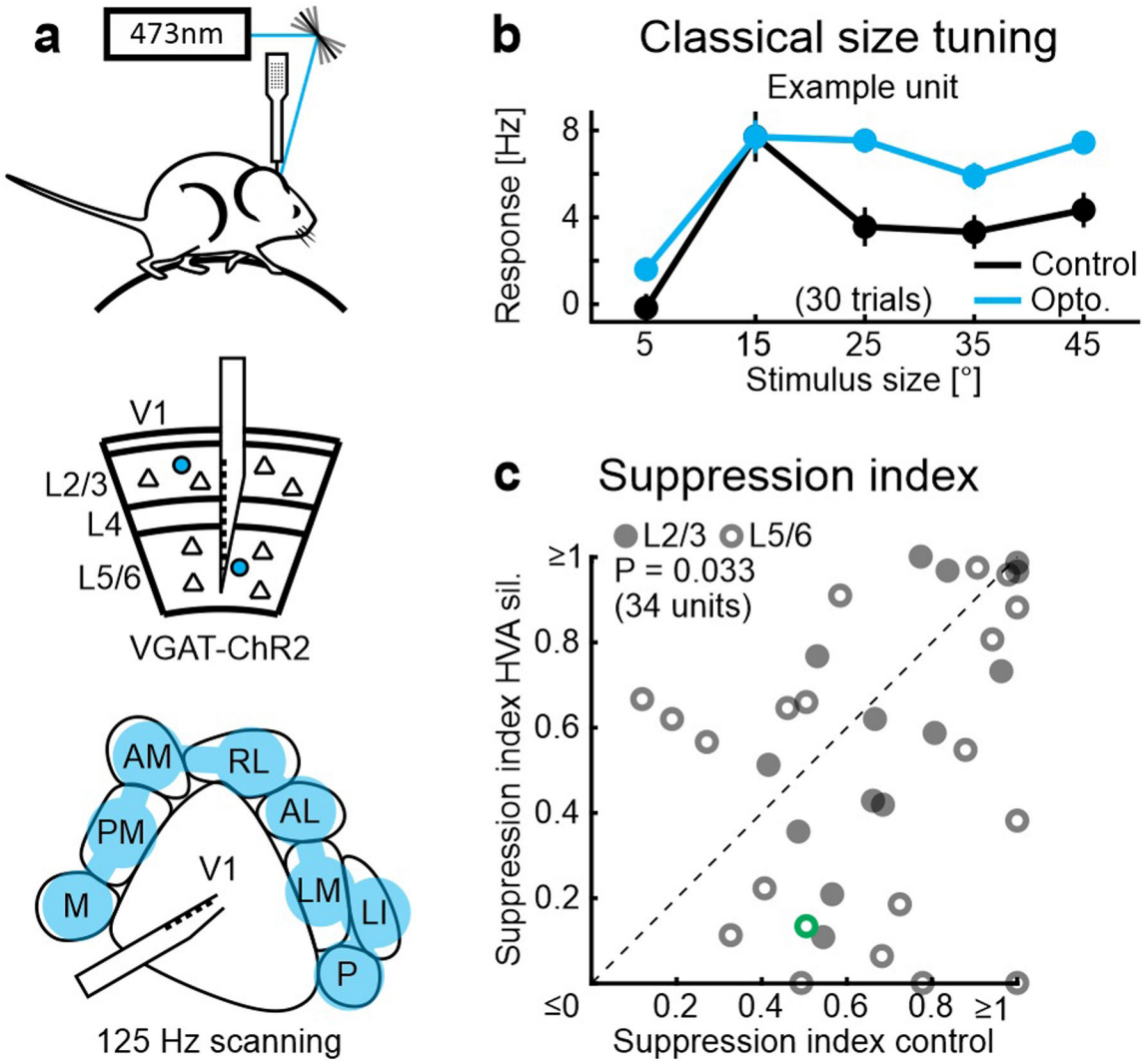

Extended Data Figure 8 |. Silencing higher visual areas reduces surround suppression in V1. **a**, Experimental configuration. A laser beam is scanned over HVAs around V1 for optogenetic silencing while recording in V1. **b**, Size-tuning function of an example unit (baseline subtracted firing rates) to classical stimuli with (blue) or without (black) HVA silencing. Note the relief of surround suppression at larger stimulus sizes upon silencing HVAs. **c**, Scatter plot of the classical suppression index with or without silencing of HVAs (see Methods). Two-sided Wilcoxon signed-rank test; p = 0.033; 34 units in 12 mice. Closed and open symbols are units from L2/3 and L5/6, respectively. Green symbol represents the example neuron shown in (**b**). Data points represent mean ± SEM.

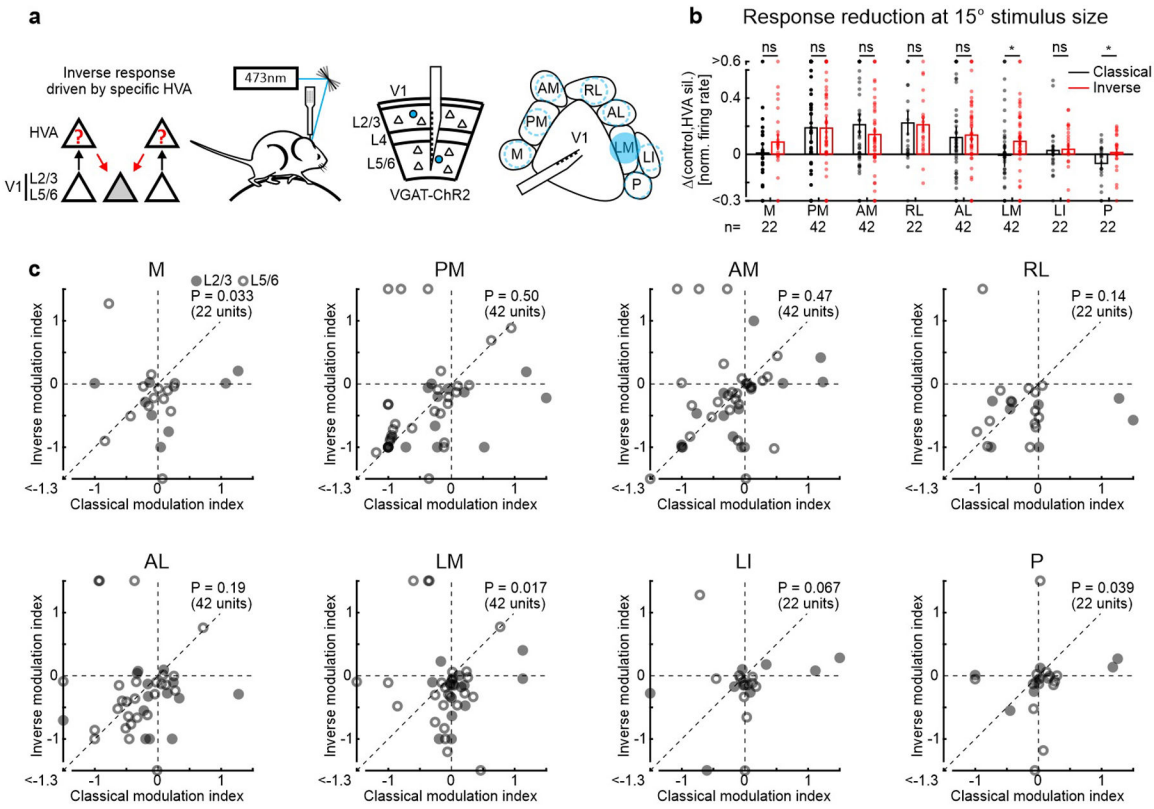

Extended Data Figure 9 |. Silencing individual higher visual areas differentially affects responses to classical and inverse stimuli.

a, Schematic of results and experimental configuration. Individual HVAs are targeted for optogenetic silencing while recording in V1. **b**, Difference in firing rates (baseline subtracted and normalized) between control conditions and individual HVA silencing for classical and inverse stimuli. Two-sided Wilcoxon signed-rank test; M, ns: p = 0.18; 22 units in 5 mice; PM, ns: p = 0.46; 42 units in 12 mice; AM, ns: p = 0.88; 42 units in 12 mice; RL, ns: p = 0.81; 22 units in 5 mice; AL, ns: p = 0.20; 42 units in 12 mice; LM, *: p = 0.013; 42 units in 12 mice; LI, ns: p = 0.51; 22 units in 5 mice; P, *: p = 0.020; 22 units in 5 mice. **c**, Scatter plot of the modulation indexes of individual HVA silencing for responses to classical and inverse stimuli (see Methods). Closed and open symbols are units from layer 2/3 and 5/6, respectively. Two-sided Wilcoxon signed-rank test; M, p = 0.033; 22 units in 5 mice; PM, p = 0.50; 42 units in 12 mice; AM, p = 0.47; 42 units in 12 mice; RL, p = 0.14; 22 units in 5 mice; AL, p = 0.19; 42 units in 12 mice; LM, p = 0.017; 42 units in 12 mice; LI, p = 0.067; 22 units in 5 mice; P, p = 0.039; 22 units in 5 mice. Note that for the visual stimulus parameters used here, LM showed the strongest effect in preferentially reducing responses to inverse stimuli. Bars represent mean ± SEM (error bars).

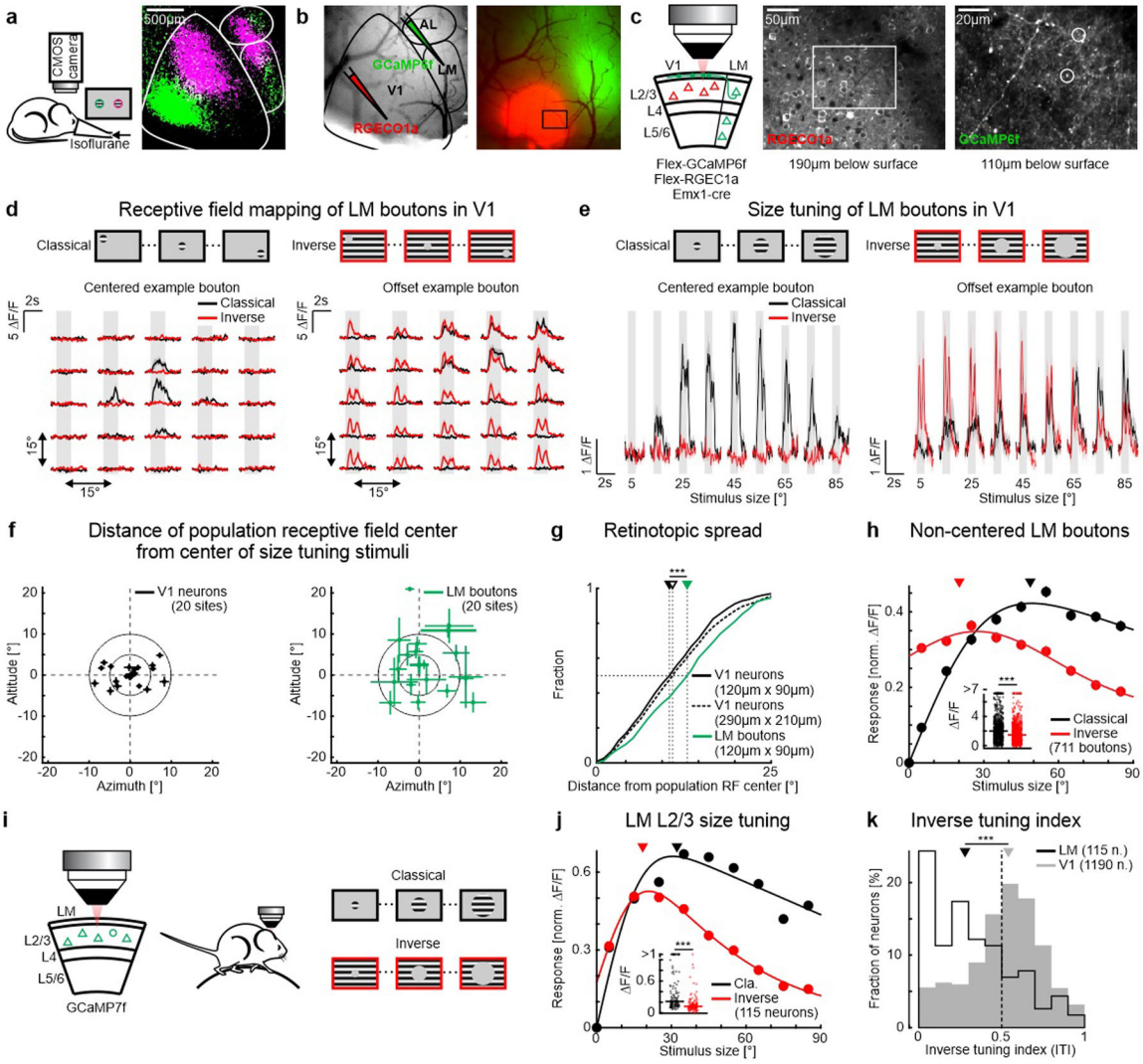

Extended Data Figure 10 |. Dual-color imaging of LM boutons and their putative V1 targets.

a, Left: Experimental configuration. To localize V1 and LM, we used intrinsic optical imaging (see Methods). Right: Response map to a nasal (magenta) and temporal patch of gratings (green). White lines represent area borders. **b**, Left: Blood vessel pattern overlaid with area borders defined by the intrinsic map (black lines). The red-shifted calcium indicator RGECO1a was injected in V1 and GCaMP6f was injected in LM. Right: Fluorescence of calcium indicators in V1 and LM. The black square delimits the example imaging site shown in (**c**). Same scale bar as in (**a**). **c**, Left: The responses of LM boutons and of V1 cell bodies were recorded within the same cortical location. Center: Example imaging site of V1 cell bodies recorded 190 µm below surface. The white square delimits the example imaging site shown on the right. Right: Example imaging site of LM boutons in V1 recorded 110 µm below surface. **d**, Top: Schematic of receptive field mapping. Left: Trial-averaged calcium responses from an example LM bouton aligned to its putative V1 target. Right: same but from an example bouton that is retinotopically offset with respect to its putative V1 target. **e**, Top: Schematic of stimuli used for size-tuning functions. Left and

right: Trial-averaged calcium responses from the same example neurons as in (**d**). **f**, Left: Distance of population-averaged receptive field center of V1 neurons from center of size tuning stimuli (20 sites in 5 mice). Right: same for LM boutons. Note that all average V1 receptive field centers are located within 10° and that average LM receptive field centers are more spread with larger standard deviations. **g**, Retinotopic spread measured as cumulative distance from population-averaged receptive field center. The ffRF centers of LM boutons (solid green line) were more retinotopically spread than V1 neurons measured over the same cortical surface (solid black line) or measured over approximately 6 times the surface of the LM bouton site (dotted black line). Two-sided Wilcoxon rank-sum test; LM-V1 same surface, ***: $p = 1.2 \times 10^{-5}$; LM-V1 6× surface, ***: $p = 3.1 \times 10^{-4}$; LM, 311 boutons in 5 mice; V1 same surface, 530 neurons in 5 mice; V1 6× surface, 2352 neurons in 5 mice. **h**, Population-averaged size-tuning function of LM boutons (711 boutons in 5 mice) that are NOT retinotopically aligned with their V1 target. Note that both classical and inverse stimuli were presented at the ffRF location of their putative V1 targets (see Methods) and NOT at the ffRF location of the imaged LM boutons. Solid lines are fits to the data (see Methods). Triangles are median preferred size. Insets: Maximum responses. Horizontal lines, medians. Two-sided Wilcoxon signed-rank test; ***: $p = 1.4 \times 10^{-11}$; 711 neurons in 5 mice. Data points represent mean ± SEM (error bars, respectively). **i**, Experimental configuration. **j**, Population-averaged size-tuning functions for classical and inverse stimuli. Solid lines are fits to the data (see Methods). Triangles are median preferred size. Insets: Maximum responses. Horizontal lines, medians. Two-sided Wilcoxon signed-rank test; ***: $p = 4.7 \times 10^{-10}$; 115 neurons in 3 mice. Data points represent mean ± SEM (error bars, respectively). **k**, Distribution of inverse tuning indices (ITIs) of LM (black) and V1 neurons (gray; same neurons as in Fig. 1c; 0: classical only; 0.5 equal peak response to classical and inverse stimuli; 1: inverse only; see Methods). Triangles above the distribution indicate medians. Two-sided Wilcoxon rank-sum test; ***: $p = 2.9 \times 10^{-15}$; 115 neurons in 3 mice and 1190 neurons in 9 mice for LM and V1, respectively.

Acknowledgements.

We thank M. Mukundan, B. Wong, and L. Bao for technical support, R. Beltramo for helping with extracellular recordings, J. Isaacson, G. Keller, R. Nicoll, and M. Heindorf for comments on the manuscript and the members of the Scanziani laboratory for helpful discussions of this project as well as for comments on the manuscript. We thank M. Rio for software support. This project was supported by the NIH grant U19NS107613, the Howard Hughes Medical Institute and the Swiss National Science Foundation grants P300PA_177882 and P2EZP3_162284 to A.J.K and P300PA_177898 to M.M.R. Confocal images were acquired at the Nikon Imaging Center at UCSF.

References

1. Hubel DH & Wiesel TN Receptive Fields, Binocular Interaction and Functional Architecture in the Cat's Visual Cortex. J. Physiol 160, 106–154 (1962). [PubMed: 14449617]
2. Pennartz CMA, Dora S, Muckli L & Lorteije JAM Towards a Unified View on Pathways and Functions of Neural Recurrent Processing. Trends Neurosci. 1–15 (2019). doi:10.1016/j.tins.2019.07.005
3. Von der Heydt R, Peterhans E & Baumgartner G Illusory Contours and Cortical Neuron Responses. Science 224, 1260–1262 (1984). [PubMed: 6539501]
4. Shen Z-M, Xu W-F & Li C-Y Cue-invariant detection of centre-surround discontinuity by V1 neurons in awake macaque monkey. J Physiol 581–592 (2007). doi:10.1113/jphysiol.2007.130294

5. Fiorani M, Rosa MGP, Gatrass R & Rocha-Miranda CE Dynamic surrounds of receptive fields in primate striate cortex : A physiological basis for perceptual completion? Proc. Natl. Acad. Sci. USA 89, 8547–8551 (1992). [PubMed: 1528860]
6. Rossi AF, Desimone R & Ungerleider LG Contextual Modulation in Primary Visual Cortex of Macaques. J. Neurosci 21, 1698–1709 (2001). [PubMed: 11222659]
7. Jones HE, Grieve KL, Wang W & Sillito AM Surround Suppression in Primate V1. Am. Physiol. Soc 2011–2028 (2001).
8. Schnabel UH et al. Figure-ground perception in the awake mouse and neuronal activity elicited by figure-ground stimuli in primary visual cortex. Sci. Rep 1–14 (2018). doi:10.1038/s41598-018-36087-8 [PubMed: 29311619]
9. Hubener M Mouse visual cortex. Curr. Opin. Neurobiol 13, 413–420 (2003). [PubMed: 12965287]
10. Niell CM & Stryker MP Highly Selective Receptive Fields in Mouse Visual Cortex. J. Neurosci 28, 7520–7536 (2008). [PubMed: 18650330]
11. Adesnik H, Bruns W, Taniguchi H, Huang ZJ & Scanziani M A neural circuit for spatial summation in visual cortex. Nature 490, 226–231 (2012). [PubMed: 23060193]
12. Angelucci A et al. Circuits and Mechanisms for Surround Modulation in Visual Cortex. Annu. Rev. Neurosci 40, 425–451 (2017). [PubMed: 28471714]
13. Walker GA, Ohzawa I & Freeman RD Asymmetric suppression outside the classical receptive field of the visual cortex. J. Neurosci 19, 10536–10553 (1999). [PubMed: 10575050]
14. Callaway EM Cell type specificity of local cortical connections. J. Neurocytol 31, 231–237 (2002). [PubMed: 12815242]
15. Dipoppa M et al. Vision and Locomotion Shape the Interactions between Neuron Types in Mouse Visual Cortex. Neuron 98, (2018).
16. Mignard M & Malpeli JG Paths of Information Flow Through Visual Cortex. Science 251, 1249–1251 (1991). [PubMed: 1848727]
17. Wang Q, Sporns O & Burkhalter A Network analysis of corticocortical connections reveals ventral and dorsal processing streams in mouse visual cortex. J. Neurosci 32, 4386–99 (2012). [PubMed: 22457489]
18. Lamme VAF, Zipser K & Spekreijse H Figure-ground activity in primary visual cortex is suppressed by anesthesia. Proc. Natl. Acad. Sci 95, 3263–3268 (1998). [PubMed: 9501251]
19. Nassi JJ, Lomber SG & Born RT Corticocortical Feedback Contributes to Surround Suppression in V1 of the Alert Primate. J. Neurosci 33, 8504–8517 (2013). [PubMed: 23658187]
20. Nurminen L, Merlin S, Bijanzadeh M, Federer F & Angelucci A Top-down feedback controls spatial summation and response amplitude in primate visual cortex. Nat. Commun 9, (2018).
21. Vangeneugden J et al. Activity in Lateral Visual Areas Contributes to Surround Suppression in Awake Mouse V1. Curr. Biol 29, 1–8 (2019). [PubMed: 30581019]
22. McDonald CT & Burkhalter A Organization Cortex of Long-Range Inhibitory Connections within Rat Visual Cortex. J. Neurosci 13, (1993).
23. Marques T, Nguyen J, Fioreze G & Petreanu L The functional organization of cortical feedback inputs to primary visual cortex. Nat. Neurosci 21, (2018).
24. Kapadia MK, Westheimer G & Gilbert CD Spatial Distribution of Contextual Interactions in Primary Visual Cortex and in Visual Perception. Am. Physiol. Soc (2000).
25. Maffei L & Fiorentini A The Unresponsive Regions of Visual Cortical Receptive Fields. Vis. Res 16, 1131–1139 (1976). [PubMed: 969225]
26. Self MW et al. Orientation-Tuned Surround Suppression in Mouse Visual Cortex. J. Neurosci 34, 9290–9304 (2014). [PubMed: 25009262]
27. Keller AJ et al. A Disinhibitory Circuit for Contextual Modulation in Primary Visual Cortex. bioRxiv (2020).
28. Gilbert CD & Wiesel TN Columnar Specificity of Intrinsic Horizontal Connections in Cat Visual Cortex and Corticocortical Connections in Cat Visual Cortex. J. Neurosci 9, 2432–2442 (1989). [PubMed: 2746337]
29. Fitzpatrick D Seeing beyond the receptive field in primary visual cortex. Curr. Opin. Neurobiol 10, 438–443 (2000). [PubMed: 10981611]

30. Peterhans E & Von der Heydt R Mechanisms of Contour Perception Contours Bridging Gaps in Monkey Visual Cortex. II. Contours Bridging Gaps. J. Neurosci 9, 1749–1763 (1989). [PubMed: 2723748]
31. Smith FW & Muckli L Nonstimulated early visual areas carry information about surrounding context. PNAS 107, 20099–20103 (2010). [PubMed: 21041652]
32. Grosof DH, Shapley RM & Hawken MJ Macaque V1 neurons can signal 'illusory' contours. Nature 365, 550–552 (1993). [PubMed: 8413610]
33. Seriès P, Lorenceau J & Frégnac Y The 'silent' surround of V1 receptive fields: theory and experiments. J. Physiol. Paris 97, 453–474 (2003). [PubMed: 15242657]
34. Knierim JJ & van Essen DC Neuronal responses to static texture patterns in area V1 of the alert macaque monkey. J. Neurophysiol 67, 961–980 (1992). [PubMed: 1588394]
35. Bastos AM et al. Canonical Microcircuits for Predictive Coding. Neuron 76, 695–711 (2012). [PubMed: 23177956]
36. Rao RP & Ballard DH Predictive coding in the visual cortex: a functional interpretation of some extra-classical receptive-field effects. Nat. Neurosci 2, 79–87 (1999). [PubMed: 10195184]
37. Keller GB & Mrsic-Flogel TD Predictive Processing: A Canonical Cortical Computation. Neuron 100, 424–435 (2018). [PubMed: 30359606]
38. Brainard DH The Psychophysics Toolbox. Spat. Vis 10, 433–436 (1997). [PubMed: 9176952]
39. Leinweber M et al. Two-photon calcium imaging in mice navigating a virtual reality environment. J. Vis. Exp 84, (2014).
40. Schindelin J et al. Fiji: an open-source platform for biological-image analysis. Nat. Methods 9, 676–682 (2012). [PubMed: 22743772]
41. Paxinos G & Franklin KBJ The Mouse Brain in Stereotaxic Coordinates Acad. Press 4th Ed., (2012).
42. Keller AJ et al. Stimulus relevance modulates contrast adaptation in visual cortex. Elife (2017). doi:10.7554/eLife.21589
43. Dombeck DA, Khabbaz AN, Collman F, Adelman TL & Tank DW Imaging Large-Scale Neural Activity with Cellular Resolution in Awake, Mobile Mice. Neuron 56, 43–57 (2007). [PubMed: 17920014]
44. Garrett ME, Nauhaus I, Marshel JH & Callaway EM Topography and Areal Organization of Mouse Visual Cortex. J. Neurosci 34, 12587–12600 (2014). [PubMed: 25209296]

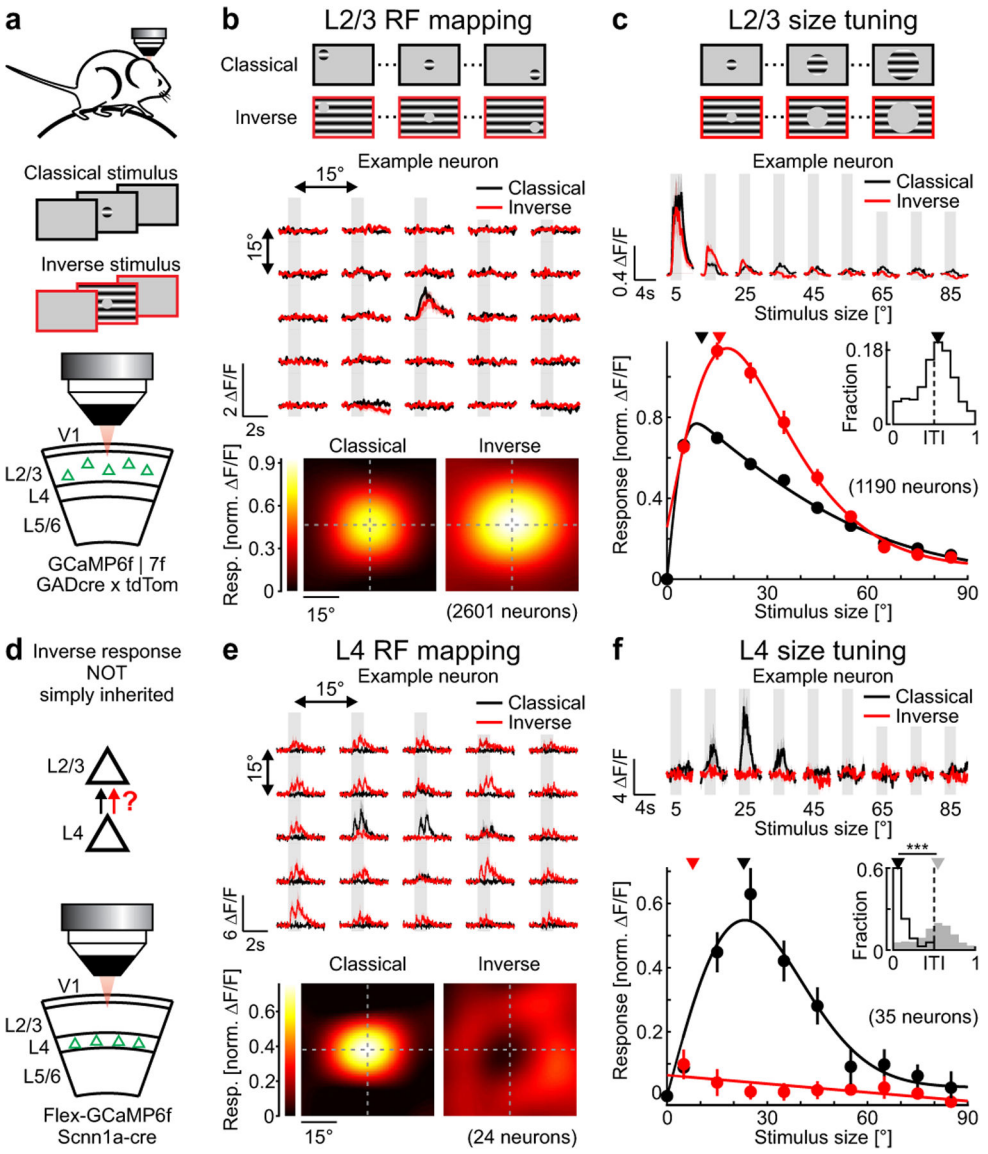

Figure 1 |. Layer-specific responses to inverse stimuli.

a, Experimental configuration. **b**, Top: Example trial-averaged calcium responses of an excitatory layer 2/3 (L2/3) neuron for each stimulus location. In all figures: shaded areas, stimulus presentation periods. Bottom: Population-averaged RFs aligned to the center of the classical feedforward RF (ffRF; 2601 excitatory L2/3 neurons in 9 mice). **c**, Top: Example trial-averaged calcium responses. Stimuli are centered on the ffRF. Bottom: Size-tuning functions, normalized to maximum response to classical stimuli. In all figures: solid lines, fits to the data; triangles, median preferred size. Inset: Inverse tuning index (ITI). Median: 0.54 (1190 excitatory L2/3 neurons in 9 mice). **d**, Schematic of results and experimental configuration. **e** and **f**, As above but for layer 4 (L4) excitatory neurons. **e**, 24 neurons in 4 mice. **f**, Inset: ITI. Median: 0.053. Two-sided Wilcoxon rank-sum test; ***: $p = 1.5 \times 10^{-18}$; black: L4, 35 neurons in 6 mice; gray: L2/3 (Fig. 1c). In all figures, traces and data points represent mean ± SEM (shading or error bars, respectively).

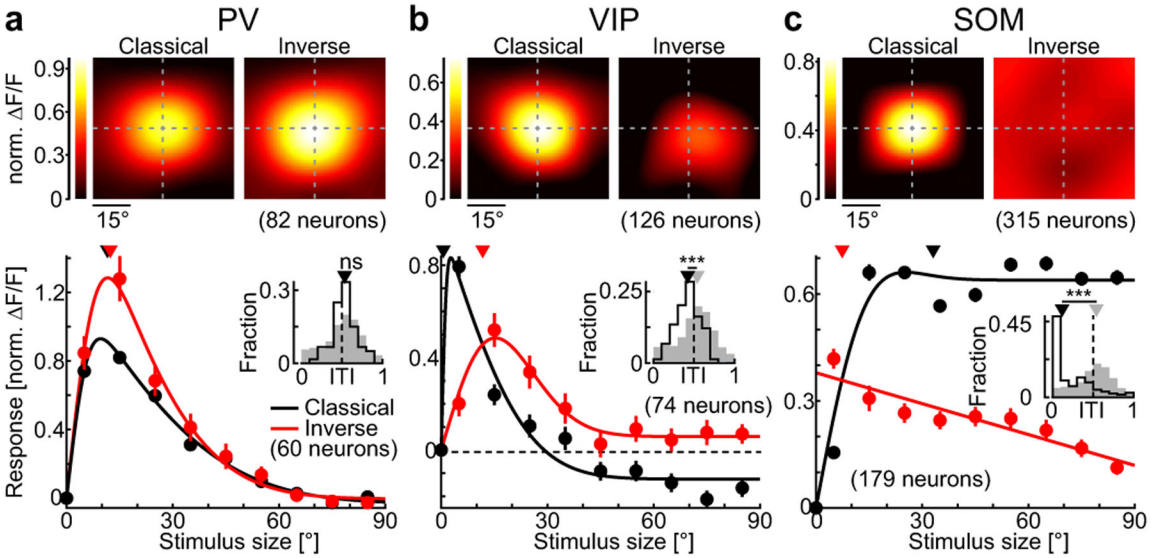

Figure 2 |. Neuron-type specific response to inverse stimuli.

a, Top: Population-averaged RF for PV neurons aligned to the center of ffRF (82 neurons in 6 mice). Bottom: Size-tuning functions, normalized to maximum response to classical stimuli. Inset: ITI. Median: 0.53. Two-sided Wilcoxon rank-sum test; ns: p = 0.79; black: PV, 60 neurons in 7 mice; gray: excitatory L2/3 (Fig. 1c). **b**, Same as in (**a**) but for VIP neurons. Top: 126 neurons in 4 mice. Bottom: Inset: ITI. Median: 0.42. Two-sided Wilcoxon rank-sum test; ***: $p = 1.1 \times 10^{-5}$; black: VIP, 74 neurons in 8 mice; gray: excitatory L2/3 (Fig. 1c). **c**, Same as in (**a**) but for SOM neurons. Top: 315 neurons in 5 mice. Bottom: Inset: ITI. Median: 0.12. Two-sided Wilcoxon rank-sum test; ***: $p = 1.1 \times 10^{-42}$; black: SOM, 179 neurons in 9 mice; gray: excitatory L2/3 (Fig. 1c).

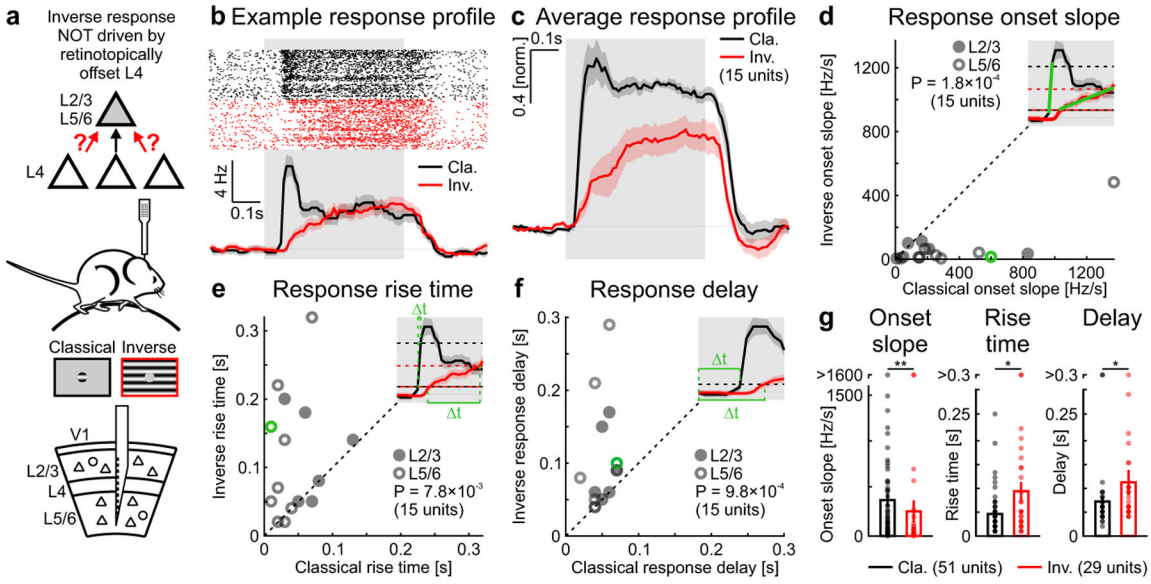

Figure 3 |. Slow and delayed responses to inverse stimuli.

a, Schematic of results and experimental configuration for extracellular recordings in V1. **b**, Responses of a layer 5/6 (L5/6) unit to classical and inverse stimuli centered on its ffRF. Top: Raster plot (1000 trials each stimulus). Bottom: Peristimulus time histogram (PSTH; 10 ms bins). **c**, Population-averaged PSTHs normalized to average response to classical stimuli (15 units in 4 mice). **d**, Onset slope of the response to classical and inverse stimuli. Green symbol, example unit from (**b**). Inset: PSTH from (**b**) to illustrate differences in slopes. Dotted lines, lower and upper thresholds to compute slopes. Two-sided Wilcoxon signed-rank test; $p = 1.8 \times 10^{-4}$; 15 units 4 mice. **e**, Same as (**d**) but for rise time. Two-sided Wilcoxon signed-rank test; $p = 7.8 \times 10^{-3}$; 15 units in 4 mice. **f**, Same as (**d**) but for delay. Two-sided Wilcoxon signed-rank test; $p = 9.8 \times 10^{-4}$; 15 units in 4 mice. **g**, Mean onset slopes, rise times, and delays of independently tuned units. Two-sided Wilcoxon rank-sum test; onset slope, **: $p = 1.1 \times 10^{-3}$; rise time, *: p = 0.017; delay, *: p = 0.031; classical: 51 units in 8 mice; inverse: 29 units in 8 mice.

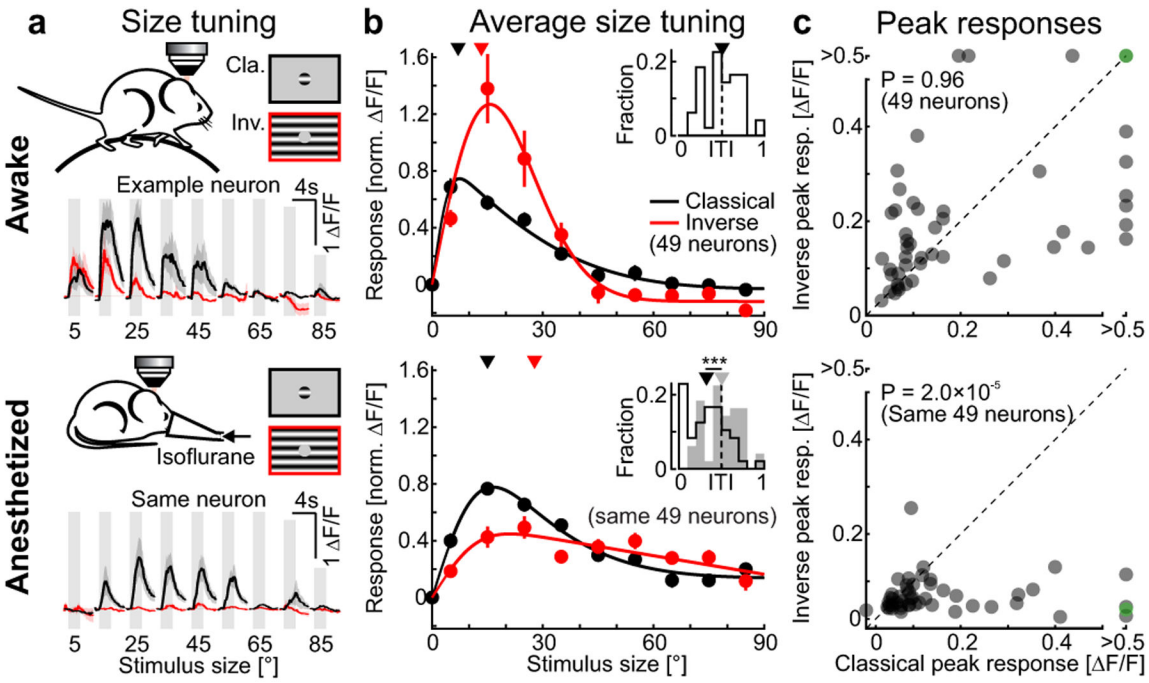

Figure 4 |. Anesthesia preferentially reduces responses to inverse stimuli.

a, Top: Example calcium responses to classical and inverse stimuli in an awake mouse. Bottom: Same example neuron but under isoflurane anesthesia. **b**, Size-tuning functions in awake (top) and anesthetized (bottom) mice, normalized to maximum awake response to classical stimuli. Insets: ITI. Top: Median: 0.50. Bottom: Median: 0.32. Two-sided Wilcoxon signed-rank test; ***: $p = 1.5 \times 10^{-5}$; black: anesthetized; gray: awake; same 49 excitatory L2/3 neurons in 5 mice. **c**, Peak responses of inverse-tuned neurons in awake (top) and anesthetized (bottom) mice. Green symbol, example neuron from (**a**). Two-sided Wilcoxon signed-rank test; top: $p = 0.96$; bottom: $p = 2.0 \times 10^{-5}$; same neurons as above.

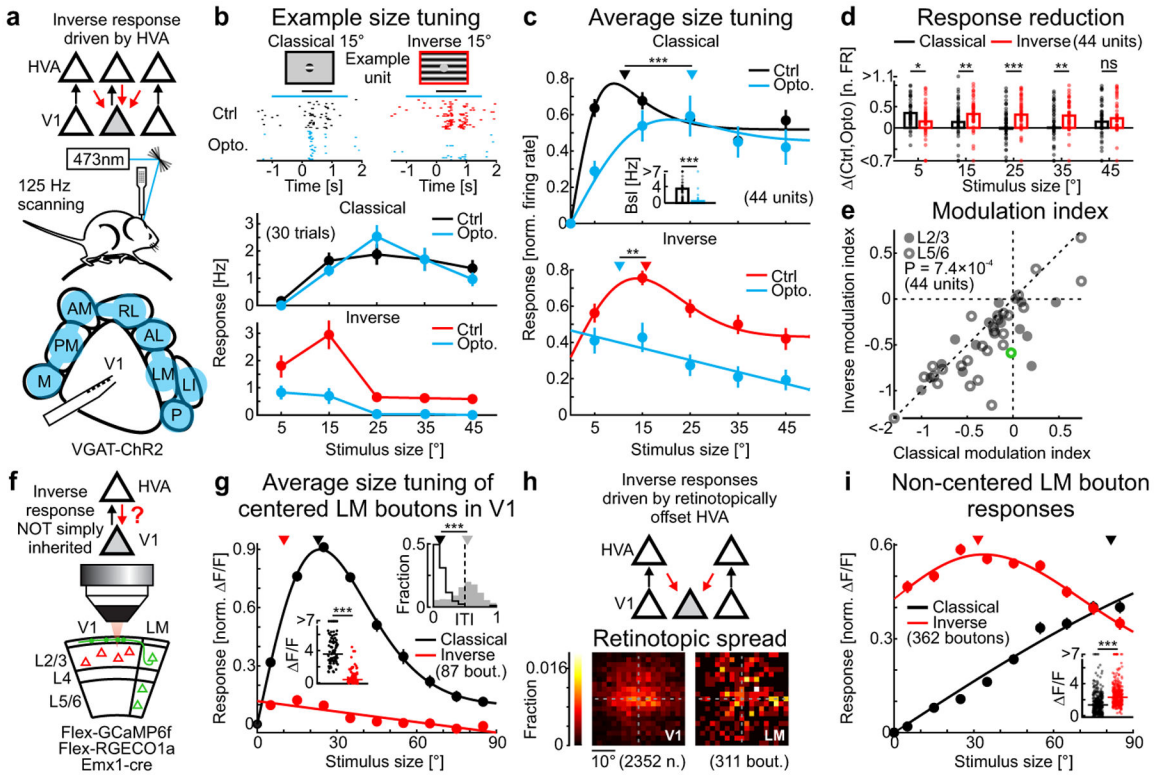

Figure 5 |. Higher visual areas contribute to inverse tuning in V1

a, Schematic of results and experimental configuration to optogenetically silence higher visual areas (HVAs). **b**, Top: Raster plot of example L5/6 unit (30 trials each). Black lines, stimulus presentation; Blue lines, HVA silencing. Bottom: Example size-tuning function with or without HVA silencing **c**, Size-tuning function with or without HVAs silencing, normalized to maximum control response to classical stimuli. Two-sided Wilcoxon signed-rank test; classical, ***: $p = 3.2 \times 10^{-4}$; inverse, **: $p = 3.0 \times 10^{-3}$. Inset: Mean baseline firing rate with or without HVA silencing. Two-sided Wilcoxon rank-sum test; ***: $p = 5.0 \times 10^{-10}$; 44 units in 12 mice. **d**, Difference in firing rates between control conditions and HVA silencing. Two-sided Wilcoxon signed-rank test; 5°, *: $p = 8.0 \times 10^{-3}$; 15°, **: $p = 1.4 \times 10^{-3}$; 25°, ***: $p = 4.0 \times 10^{-5}$; 35°, **: $p = 3.5 \times 10^{-3}$; 45°, ns: $p = 0.70$; 44 units in 12 mice. **e**, Optogenetic modulation indexes (see Methods). Green symbol, example neuron from (**b**). Two-sided Wilcoxon signed-rank test; $p = 7.4 \times 10^{-4}$; 44 units in 12 mice. **f**, Schematic of results and experimental configuration. **g**, Size-tuning function for LM boutons retinotopically aligned to their putative V1 targets. Insets: Left: Maximum responses. Horizontal lines, medians. Two-sided Wilcoxon signed-rank test; ***: $p = 6.1 \times 10^{-16}$. Right: ITI. Median: 0.11. Two-sided Wilcoxon rank-sum test; ***: $p = 2.8 \times 10^{-38}$; black: LM, 87 boutons in 5 mice; gray: L2/3 (Fig. 1c). **h**, Top: Schematic of results. Bottom: Retinotopic spread of the ffRF of V1 neurons and LM boutons (2352 neurons and 311 boutons in the same 5 mice). **i**, Size-tuning functions of LM boutons not retinotopically aligned with their putative V1 targets. Inset: Maximum responses. Horizontal lines, medians. Two-sided Wilcoxon signed-rank test; ***: $p = 4.8 \times 10^{-36}$; 362 boutons in 5 mice.